FOAMING KINETICS OF CLOSED CELL RIGID POLYURETHANE FOAM

A Thesis
Submitted to the Graduate Faculty
of the
North Dakota State University
of Agriculture and Applied Science

By

Kimberly Nicole Meyer

In Partial Fulfillment of the Requirements
for the Degree of
MASTER OF SCIENCE

Major Program:
Mechanical Engineering

October 2010

Fargo, North Dakota

North Dakota State University
Graduate School

Title

Foaming Kinetics of Closed Cell

Rigid Polyurethane Foam

By

Kimberly Nicole Meyer

The Supervisory Committee certifies that this ***disquisition*** complies with North Dakota State University's regulations and meets the accepted standards for the degree of

MASTER OF SCIENCE

SUPERVISORY COMMITTEE:

ABSTRACT

Meyer, Kimberly Nicole, M.S., Department of Mechanical Engineering, College of Engineering and Architecture, North Dakota State University, October 2010. Foaming Kinetics of Closed Cell Rigid Polyurethane Foam. Major Professors: Dr. Chad A. Ulven, Dr. Iskander Akhatov.

Rigid polyurethane foams have shown promise in several applications as a means to reduce weight without compromising structural properties. Information about the chemical formula of the liquid components, the reaction to produce foaming, and the curing kinetics of rigid polyurethane foam are discussed. The chemical formulas of the liquid components are described, and the reaction required to produce foaming and cure of the polyurethane is stated. The foaming kinetics of the polyurethane were determined based on experimental work as well as theoretical modeling. It was determined that there was a relationship between the initial load the frame was placed under and the amount of pressure measured during the foaming process. The theoretical modeling was conducted for an equilibrium scheme as well as viscosity and diffusion controlled stages. Each of the models predicted the bubble growth to be much quicker than was seen in experimental work, but captured dimensional properties in the foam. The curing kinetics of the liquids and thermal profile of the foaming reaction were measured and a plan for incorporation into future modeling is discussed.

ACKNOWLEDGMENTS

I would like to thank my advisers, Dr. Chad Ulven & Dr. Iskander Akhatov, for all their advice, assistance, guidance, and time spent throughout this research project. It was an honor being their graduate student. My appreciation is also extended to Dr. Alan Kallmeyer and Dr. Jing Shi. I thank them for the advice, assistance, and contribution to this committee. I would like to thank Aron Fisk, Luke Gibbon, Nicholas Goenner, Loren Soma, and the other members of our research group for the lab and equipment help within this project. A sincere thank you also goes out to my husband and family for their love and support during this time.

I cannot forget that without the financial support of this research project from SpaceAge Synthetics Incorporated and the U.S. Navy my research would not have been possible.

TABLE OF CONTENTS

LIST OF TABLES

LIST OF FIGURES

Page

Figure

LIST OF VARIABLES

α.....degree of conversion

c.....equilibrium gas concentration in the cell liquid

c_f.....specific heat of the foam

c_0.....initial concentration of gas dissolved before foaming

c_s.....concentration of gas dissolved in liquid at normal conditions

c_* .....critical concentration value

D.....diffusion coefficient

$\delta(t)$.....thickness of diffusion boundary layer

E_a.....activation energy

H.....Henery's Law constant

h_B.....thickness of bottom plate

h_T.....thickness of top plate

H_{total}.....total heat of reaction

h_0.....initial liquid height

h_1.....final thickness of the foam

k_B.....thermal conductivity of the bottom plate

k_f.....thermal conductivity of the foam

k_T.....thermal conductivity of the top plate

m_g.....mass of gas in bubble

m_l.....mass of liquid contained in a single bubble

μ.....liquid viscosity

n_0.....number of gas nuclei per unit mass liquid

p_{atm}.....atmospheric pressure

p_f.....foam pressure

p_g.....gas pressure in bubble

q.....heating rate

r.....radial coordinate

R_b.....average final bubble radius

R_{b1}.....minimum bubble size

R_{b2}.....maximum bubble size

R_c.....cell radius

R_g.....CO_2 gas constant

R_0.....cell radius at normal conditions before bubble nuclei is generated

ρ_f.....foam density

ρ_{g^*}.....gas density at normal conditions

ρ_l.....liquid density

σ_{rr}.....radial component of stress

T.....temperature at a point in time

T_0..... initial (room) temperature

$u_l(r,t)$.....radial liquid velocity

CHAPTER 1. INTRODUCTION

Recently, a growing emphasis has been placed on reducing the size and weight of automobiles in order to improve gas mileage and decrease the money spent on buying gasoline. Vehicles began as large, heavy, metal structures which served their purpose, but are now being seen as grossly over-designed. In the last several years, there has been a shift towards using lighter weight materials for several components in an automobile in an effort to reduce the vehicle's overall weight. Similarly, the United States Navy is also looking to reduce weight of their heavy, bulky ships. The implementation of lighter weight materials in these ships will help improve their maneuverability, speed, and allow for greater payload or fuel capabilities. The most promising materials being investigated for implementation are composite materials. These materials can be optimized for strength, stiffness, and dynamic loadings in the directions needing these properties, while still achieving substantial weight savings over metals.

A collaborative research project between North Dakota State University (NDSU), SpaceAge Synthetics, Inc. (SAS) of Fargo, ND and the U.S. Naval Undersea Warfare Center Division (NUWCD) has been established to develop applications of SpaceAge Synthetics, Inc. Thermo-Lite composite materials for the U.S. Navy's unmanned surface vehicles (USVs) and mission modules program. The Thermo-Lite composite material is a commercial product of SpaceAge Synthetics, Inc. and is a lightweight, pseudo-sandwich

composite material, containing a rigid polyurethane polymer matrix reinforced with various glass fiber architectures. This project required extensive material property evaluation through a variety of mechanical testing and characterization. Additional testing, including foaming kinetics, fire studies, accelerated weathering, as well as high and low velocity impact studies have led to a greater knowledge of the Thermo-Lite material.

One of the unmanned surface vehicles initially identified for application of the Thermo-Lite material was the Spartan Scout, pictured in Figure 1. The Spartan Scout is a Rigid Hull Inflatable Boat (RHIB) weighing two tons and is reconfigurable to adapt to various missions as set forth by the NAVY and NUWCD. The various missions outlined for the Spartan are Precision Strike (PS), Mine Identification Warfare (MIW), and Force Protection/Intelligence, Surveillance and Reconnaissance (FP/ISR).

As currently designed, the weight of the Spartan Scout exceeds the lifting capacity of the loading/unloading cranes installed on the littoral combat ships (LCS). These cranes are used to lift the USV into the water at the start of a mission. With the currently designed vessels being so overweight, the USV needs to be emptied of fuel to be lifted by the cranes and deployed in the water. Emptying and refueling of the USV takes extra time and manpower to ready the craft for service. By reducing the weight of several components of the USV the time needed to fill with fuel will be lessened or even eliminated.

Figure 1. The U.S. Navy unmanned surface vehicle (USV) Spartan Scout [1].

Thermo-Lite composite material can be designed to meet the varying structural sheeting applications of the Naval USVs; however, little work has been done on predicting how the material will perform with a complex geometry. Therefore, the scope of this body of work is to study the foaming kinetics of rigid polyurethane foam based composites and develop means to predict their processing characteristics. A thorough knowledge of the experimental research done in this field will help to more fully understand the effect that foaming has on final material properties as well as allowing further optimization in the future.

1.1. Foam Materials

The primary attribute of a foamed material is its low density; nearly 75-95% of the volume may be void space when compared to the solid base material. Applications of foams are in impact absorption as in bike helmets, insulation materials for space shuttle applications, and chemical filters using micro or nano-sized open celled foams [2]. The following sections provide information on the various types of materials manufactured with a foamed structure along with the types of pore structures achievable with current manufacturing processes.

1.1.1. Material Types

The majority of commercially available foam materials fall into three main categories: metallic foams, ceramic foams, and polymer foams. Metallic foams are becoming increasingly popular with the improvement in manufacturing capabilities. Benefits of this type of foam are its ability to be recycled back to the base material by melting, and its retention of a similar thermal expansion as the base material. A limitation, however, is when a metal is used in the foamed state, it sees a reduction in its electrical conductivity. Ceramic foam can also be recycled back to the base material and is typically used for thermal insulation or as a filter for hot gasses.

Nearly all thermoplastic and thermoset polymers can be manufactured into a foam material. As with the base material, thermoplastic foams can be recycled back to their original form while thermosets are permanently cross-linked and cannot be further modified. More recent foams are including additives to increase the strength, modulus, and fracture toughness of composite foams.

1.1.2. Pore Structures

Within the broad category of foam materials, there are several cell types that can be manufactured: open cell, closed cell, and syntactic foams. An open cell structure contains pores that are connected to each other and form an interconnected network while a closed cell structure contains pores which are not connected. A less common foam type is syntactic foam. This type of foam consists of hollow spheres embedded in a matrix material. A picture of a typical open cell structure, closed cell structure, and syntactic foams can be seen in Figure 2.

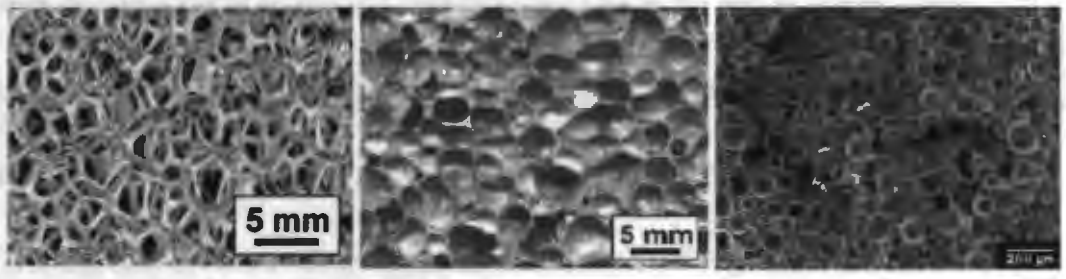

Figure 2. Open Cell Structure, Closed Cell Structure, Syntactic Foam [3].

Closed cell structures, when compared to open celled structures, typically have higher compressive strengths, are better insulators, and have a higher density. In a closed cell material, gas is contained inside each of the pores rather than being able to freely pass through as in an open cell material. This trapped gas increases the materials ability to thermally insulate as well as acting as a sound barrier. The extra material forming the walls in a closed cell foam is what gives the material its increased compressive strength and density. The hollow spheres in the syntactic foam reduce the overall density of the matrix material, but they typically have the largest density of the three foam types. The hollow spheres may also give the composite foam an increased strength depending on the interfacial bonding between the sphere particles and the matrix. These foams can be easily tailored for their specific application based on the volume fraction, size, material, and the gas which fills the hollow spheres. Syntactic foams are typically used in applications where weight savings are needed in a structure that has the potential to be in service with or near a water source. An example would be in the hull of a boat, where weight savings would result in less fuel consumption and the foam would have the potential to absorb water. Each of these foams is created by a different manufacturing process to obtain the difference in their structure. Research has been conducted to determine the effect of pore size and shape on the properties of the final foamed material [4-8]. The mechanical properties of cell walls were found to vary significantly because of

irregular geometries and inconsistent microstructures. Cell face curvatures and corrugations were found to decrease the elastic modulus and plastic collapse stress in metallic foam materials [9].

1.1.3. Cell Measurement

With foams having variances in their cell size, wall thickness, and other geometrical features a difficulty arises when obtaining an accurate measurement of these cells. Whether used in research or the need for precision and tight tolerances of mass produced foams, dimensional and geometrical measurements is becoming an ever necessary tool. Several methods have been examined to characterize cell size and topography, such as light transmission [10], x-ray tomography [11,12], scanning electron microscopy (SEM) [13], magnetic resonance imaging (MRI) [14], photography [15], and 3D optical methods [16]. The 3D optical method uses three two-dimensional images to generate a stereo representation of a portion of the foam surface. Several of these images are captured at different view angles and combined into one set of points. A computer software program is then used to create the foam structure based on these captured points. Each of the methods have limitations due to the foam material and pore size of the material being measured. For example, and optical measurement system has a limited accuracy depending on the mega-pixels of the camera and its field of view.

1.2. Polyurethane

1.2.1. History

The origin of polyurethane dates back to World War II where it was first created in Germany as a replacement for rubber, a scarce material at that time. Today, polyurethanes can be found in nearly all items used daily – desks, cars, chairs, clothes, footwear, appliances, beds, the insulation in walls, roof and moldings on homes. Polyurethanes can be created in many forms, such as: liquid coatings, paints, elastomers, rigid insulation, or soft flexible foam. Rigid polyurethane foams form one of the world's most popular, energy-efficient, and versatile insulations, which significantly cuts fuel and construction costs [17].

1.2.2. Chemistry

Polyurethanes consist of repeating organic units joined by urethane links, which are polymerized via step-growth polymerization. This two-part liquid resin system consists of an isocyanate and a polyol, which react to form the final polyurethane product. Isocyanates are a highly reactive, low molecular weight compounds. Diisocyanates, or compounds containing two isocyanate groups, are most often utilized in the production of polyurethane foams [17]. A polymeric methylene diphenyl diisocyanate (PMDI) type isocyanate is used for this work, with its structure shown below.

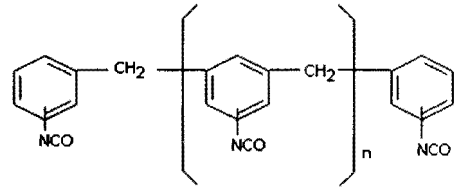

Figure 3. Chemical structure of
PMDI isocyanate [18].

Polyols are an alcohol with more than two reactive hydroxyl groups per molecule [17]. An ester type polyol is used in this work, which is capable of forming more hydrogen bonds and leads to an improved interchain interaction and elastic properties [19]. Polyurethane is formed by the polymerization reaction of an isocyanate with a polyol in the presence of suitable catalysts and additives [17], as seen in Figure 4. Because a wide range of diisocyanates and a variety of polyols can be used to produce polyurethane, a broad array of materials can be produced to meet the needs of specific applications [17]. It can be formulated for a wide range of stiffness, hardness, and density, based on the formulation of the constituents.

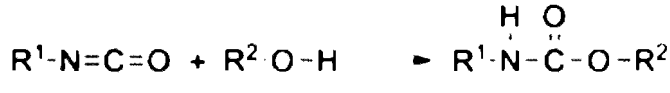

Figure 4. Generalized polyurethane reaction [20].

Most polyurethane are thermosets, though it can also be created as a thermoplastic. Thermosetting polyurethanes are used in applications such as molds, tools, dies, wheels,

adhesives, sealants, or structural foams. Thermoplastic polyurethane (TPU) is an elastomer that is fully thermoplastic, or able to be melt processed. Its applications include: flexible tubing, hydraulic hoses & seals, inflatable rafts, medical tubing, swim fins & goggles, and wire & cable coatings [17].

1.2.3. Blowing Agents

In order to create the pores found in a foamed polymer a blowing agent must be used. A blowing agent is a substance when used alone or in combination with other substances is capable of producing a cellular structure in a material. Blowing agents may include compressed gases that expand when pressure is released, liquids that develop cells when they change to gases, soluble solids that leave pores when leached out or chemical agents that decompose or react under the influence of heat to form a gas. A common use of a blowing agent is to supersaturate a gas into the liquid resin under pressure and when the pressure is released, bubbles form and grow [21]. The type of blowing agent used has a significant effect on the long-term stability of the foam structure and insulating properties of the foam as well as other aspects such as the load bearing capability, cushioning effect, or flammability of the foam. The insulating achieved by a foamed product is determined by the thermal conductivity of the gas phase of the blowing agent within the pores as well as the cell wall thickness. Due to environmental concerns with some types of blowing

agents, there are global and regional guidelines in place to monitor and suggest the discontinued use of a blowing agent if a concern should arise.

The polyurethane used for this research is formulated such that the reaction does not use a harmful chemical blowing agent. Instead, water is grafted onto a polyol monomer and when allowed to react with the isocyanate, gives off carbon dioxide gas to form the cellular structure. This formation of gas produces pockets of carbon dioxide gas that remain entrapped in the material once it solidifies. These entrapped gas pockets are the pores seen in closed cell foams. This interaction is shown in Figure 5 with the disubstituted urea being the final polyurethane product.

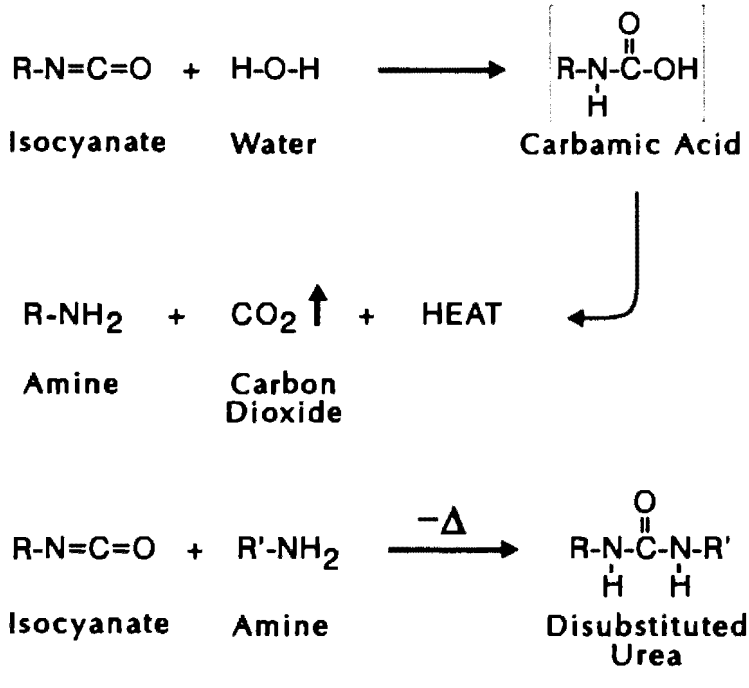

Figure 5. Reaction of water with polyol to form carbon dioxide gas [22].

With the variety of formulations of polyurethanes currently available, much analysis has been done characterizing it in its many forms [23-41]. To determine which variety of polyurethane is to be used will depend upon the parts intended application. Polyurethane foams are used in applications from soft cushioning to structural sheeting. The structural sheeting industry uses a rigid, closed cell, polyurethane foam, which is the focus of this research.

1.3. Foaming Kinetics

Much work has been done to determine the way in which several materials obtain their cellular structure [42-50]. With a broad range in materials; such as metals, polymers, and even bread dough, there is a large range of ways in which these substances become a foamed material. In order to model a foaming liquid, a simplified picture of the foaming process needs to be created. Several theoretical models have been created to try and model the foaming behavior by quantifying the surface tension, viscous, and inertial forces which slow down the rate of increase of bubbles in a viscous liquid [51-55]. Other models have been created which deal with a single bubble in an infinite sea of liquid [56-59]. This has been shown to be an unacceptable model for bubbles that are eventually separated by distances that are short in comparison with their radii. This model may be used as an

approximate representation of the very early stages of foam expansion, but deviates from reality in the later stages of the foaming process.

CHAPTER 2. OBJECTIVES

Over the past decade, composite materials have become increasingly popular in the automotive, construction, marine, and transportation industries. More specifically, foam core sandwich structures are used in a large variety of applications due to their high stiffness and low weight. In order to design with these materials, a thorough understanding of their material properties and cellular geometry needs to be examined. The manufacturing parameters such as temperature, pressure, and time, play a large role in the final properties of a foamed polymer product. These parameters may affect the pore size, wall thickness, or other geometries of the cellular structure. In order to understand the final pore geometry a part will obtain, knowledge of the foaming process needs to be clearly understood.

Therefore, the objectives of this research were to:

- Determine the final average cell size and rate of change with time.
- Find time of foam growth required to fill a mold.
- Cooling time required for demolding.
- Find the pressure generated due to a volume of liquid expanding.
- Create codes for prediction of final bubble radius that allow for manipulation of initial parameters.

CHAPTER 3. EXPERIMENTAL SETUP

This section outlines the overall experimental procedures, a schematic of the experimental setup, and the testing conditions used. Details on the method of replicating tests are also stated. This work was modeled after the manufacturing process used at SpaceAge Synthetics, Inc. in order to correlate the results as closely as possible.

3.1. SpaceAge Synthetics, Inc. Manufacturing Process

The manufacture of composite Thermo-Lite boards is accomplished at SpaceAge Synthetics, Inc. in Fargo, ND. The Thermo-Lite composites consist of varying architecture of glass, which is later impregnated with the polyurethane foam and allowed to expand to take the form of the mold in which it is placed. An E-glass is used in the Thermo-Lite material in several forms: continuous fiber mat (CFM), woven roving, and a lightweight glass filter. Each of the glass types in a commonly used stacking sequence along with the final product can be seen in Figure 6.

The varying types of E-glass are stacked into a rectangular 1.22 meter by 2.44 meter frame which varies from 9.53 to 50.8 millimeters thick. The bottom mold is constructed of steel or a medium density fiberboard (MDF) material, depending on the press in which the product is manufactured. An overhead sprayer mixes the polyol and

isocyanate liquids and sprays them evenly onto the glass loading. The top of the mold, a flat steel plate, is quickly put in place and 1 MPa of pressure is used to ensure the mold remains shut. Several vents are machined into the mold to allow the air initially inside the mold to escape so air pockets are not created in the surface of the part.

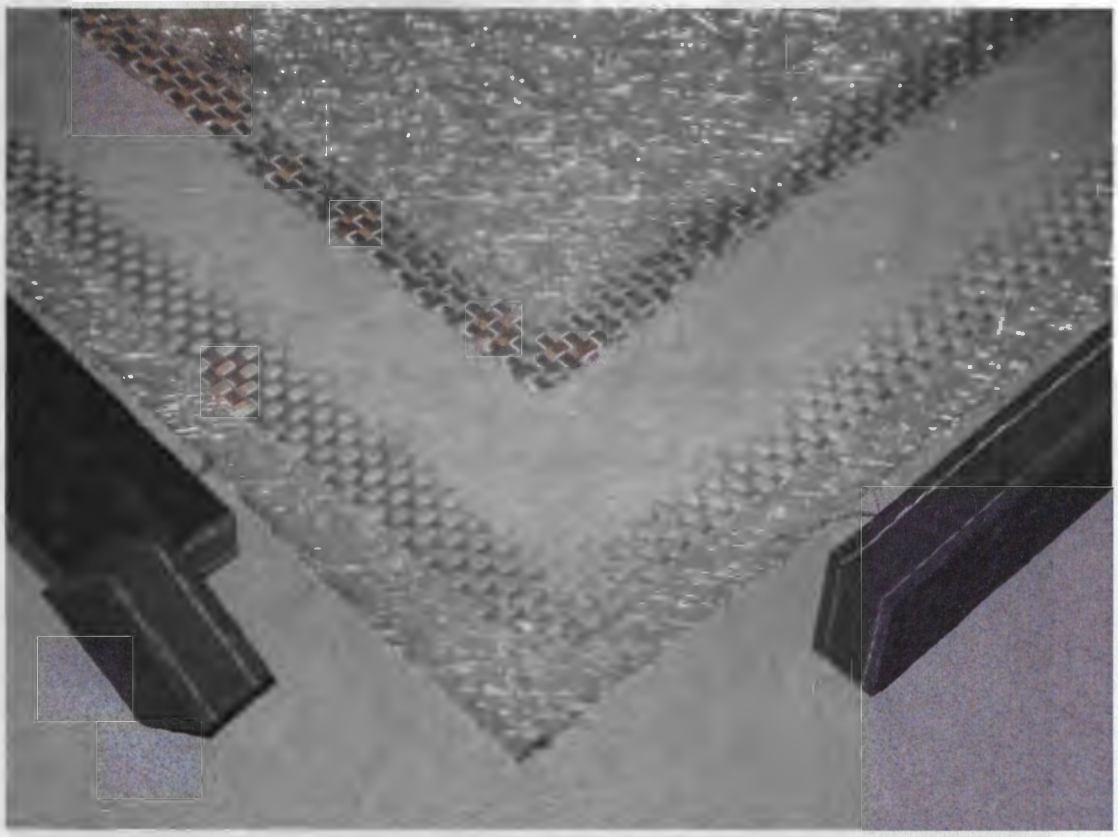

Figure 6. E-glass stacking sequence.

3.2. Testing Apparatus

The apparatus used for this work was made of steel and consisted of a square frame placed between two flat plates. Three frames were used for the research, having the dimensions listed below.

Table 1. Frame dimensions.

Frame	Inner Length	Inner Width	Frame Thickness	Height
	cm	cm	cm	cm
A	10.16	10.16	0.635	1.27
B	10.16	10.16	1.27	1.27
C	40.64	40.64	2.54	2.54

The two small frames contain the same inner foaming area, the difference being the width of the frame. A picture of each of the frames are shown in the following figures.

Figure 7. Frame A (left) and frame B (right).

The small frames contained an opening for an injection site used to transfer the liquid into the mold and a thermocouple probe to be placed into the mold. The liquid for the large frame was injected into the mold cavity through an opening in the top plate of the apparatus. For each of the frames, the top and bottom plates were made of 1.27 cm thick steel.

Figure 8. Frame C.

The top and bottom plates for Frames A & B also contained a conductive heat flux sensor to measure the heat flux at the interface. A schematic of the side-view of this setup is shown in Figure 9.

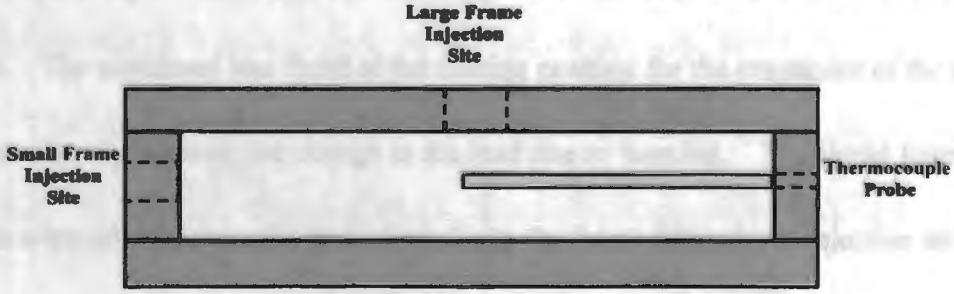

Figure 9. Schematic of experimental setup.

The small frame was used for the first sets of experiments, while the large frame was used to scale up the experiment and check for consistency. Having two frame widths for the small frame was done to examine if there were any size or edge effects due to the variance in surface area.

3.3. Equipment

The testing of the small and medium frames were accomplished on an Instron 5567 load frame machine. The larger frame was tested on a Tinius Olson load frame due to the larger testing apparatus and loads required.

3.4. Testing Method

3.4.1. Frames A & B

The tests were run with the 10.16 cm x 10.16 cm x 12.7 mm frame sandwiched between the top and bottom plates, with the entire system positioned in the Instron load frame. An initial load was applied and the apparatus was left under the load for several minutes to come to equilibrium. The stabilized load was recorded as the initial load for the experiment. The crosshead was fixed at the starting position for the remainder of the test in order to accurately measure the change in the load due to foaming. The liquid foam components were mixed externally and injected into the frame through the injection site in the side of the frame. The injection site was then sealed shut for the remainder of the

experiment. The edges of the mold had small vents to allow for the air initially trapped inside the mold to escape while keeping the amount of liquid escape (i.e. flash) to a minimum. The time of injection for the mixed liquids was used as the starting time for the experiment. The apparatus was left to foam and load measurements were taken twice a second for thirty minutes. Several initial loads were examined in order to examine the effect on the resulting measured foam pressure. A large enough preload was needed in order to limit the amount of foam escaping from the mold.

3.4.2. Frame C

The tests were run with the large frame sandwiched between the top and bottom plates, both made of 12.7 mm plate steel. The entire system was then positioned in the Tinius Olson load frame and an initial preload was applied. The apparatus was left under load for several minutes to come to equilibrium and the stabilized load was recorded as the initial load for the experiment. The crosshead was again fixed at the starting position for the remainder of the test. The liquid foam components were mixed externally and poured into the frame through the injection site in the top plate of the mold. The injection site was then sealed. The time of injection for the mixed liquids was used as the starting time for the experiment. The polyurethane was left to react at room temperature, with load

measurements being measured every ten seconds for two minutes and a final reading being taken at thirty minutes.

3.5. Thermal Profile

The thermal profile of the reacting foam was measured using several thermocouples inserted into a container of foaming polyurethane. Four, Type K thermocouples were placed into a plastic cup containing the pre-mixed liquids to measure the temperature evolution over time. The temperatures were measured in the positions shown in Figure 10. These locations were chosen to examine the temperature profile across the diameter of the cup as well as the height effects.

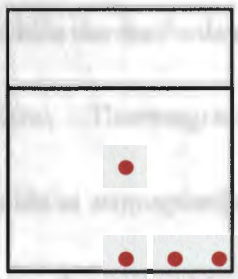

Figure 10. Thermocouple locations.

3.6. Heat Flux

In order to examine the effect the top and bottom plate material played in the thermal profile within the curing polyurethane, a heat flux sensor was used. Using Frame A and Frame B, a thin film conductive heat flux sensor was embedded in the top and

bottom plates and the heat flux was measured during the curing reaction. The measurements were taken twice a second for thirty minutes. The Omega HFS-4 heat flux sensor has a thickness of 0.2286 mm and gave a response time of 0.7 seconds. Also contained in the sensor is a type K thermocouple for measuring the temperatures at the top and bottom plate interface. Heat flux and temperature measurements were taken for plates made of steel as well as plates made of MDF wood composite.

3.7. Polymerization Kinetics

For the polyurethane system examined in this research, both foaming and polymerization of the liquids happen simultaneously. The foaming process is examined in further detail in the following chapters, while the methods employed to examine the polymerization kinetics are discussed below. Thermogravimetric analysis was conducted to examine the moisture levels in the liquids at atmospheric conditions, while differential scanning calorimetry was used to determine the curing kinetics. These analyses are described in detail below.

3.7.1. Thermogravimetric Analysis

A TA Instruments Q500 thermogravimetric analyzer (TGA) was used to determine the percentage moisture in the polyol and isocyante liquids at normal conditions. The TGA measures the weight change in a material as a function of time or temperature under a

controlled environment. A drop (50-80 mg) of each of the liquids were put into 50 μL platinum sample pans and placed into the sample carousel. An autosampler weighed the reference pan and brought the samples into the chamber for each of the tests. Two of the samples were heated from room temperature to 800 °C at a rate of 10 °C per minute, while the other samples were heated to 120 °C and held for sixty minutes and then heated to 800 °C at 10 °C per minute. Two samples of each of the liquids were tested using the same procedure to ensure accuracy of results.

3.7.2. Differential Scanning Calorimetry

In order to determine the rate of polymerization, differential scanning calorimetry (DSC) was used to measure the chemical conversion in the curing polyurethane by evaluating the heat evolution caused by the exothermic reaction. This was accomplished using a TA Instruments Q1000 DSC machine. The two polyurethane liquid components were mixed, 5-15 mg were injected into an aluminum pan, the edges crimped to encapsulate the sample, and rapidly transferred into the DSC machine, all within 30 seconds. In order to keep the polyurethane from expanding outside of the crimped pan, the foaming agent (water) was previously removed from the polyol during a 60 minute heating cycle. A small, aluminum reference pan and the pan containing the polyurethane liquid were brought into the isolated furnace and positioned by an automatic arm. Once the

chamber came to the correct starting temperature the run began, heating the sample for the desired heating cycle. Several heating cycles were conducted in order to obtain the activation energy and rate of cure. The samples were heated from -5°C to 200°C at a rate of 5°C/min, 10°C/min, 15°C/min, or 20°C/min. The samples were heated at the desired rate and the heat flow was measured.

CHAPTER 4. EXPERIMENTAL RESULTS & DISCUSSION

4.1. Experimental Testing

4.1.1. Foaming Pressure Determination

Testing was conducted on each of the three frames to determine the amount of pressure created during foaming of a panel with densities ranging from 0.39-0.44 g/cm^3. First, Frame A was used with several preload values to examine the pressure created during foaming. Then, Frame B was used to determine if there were any edge effects, and Frame C was used to examine the results of scaling up the experiment. The results are described in detail in the following sections.

4.1.1.1. Frame A

Tests were run on Frame A at preloads varying from 3.5 – 10 kN with replicates at 6 kN to verify repeatability. For each of the tests 78.5 grams of the mixed polyurethane liquids were injected into the mold. The initial pressure due to the preload acting on the frame as well as the final pressure on the foamed area were measured. The density of the final sample was found and the amount of material that escaped from the mold was noted. A typical time versus pressure plot is shown in Figure 11.

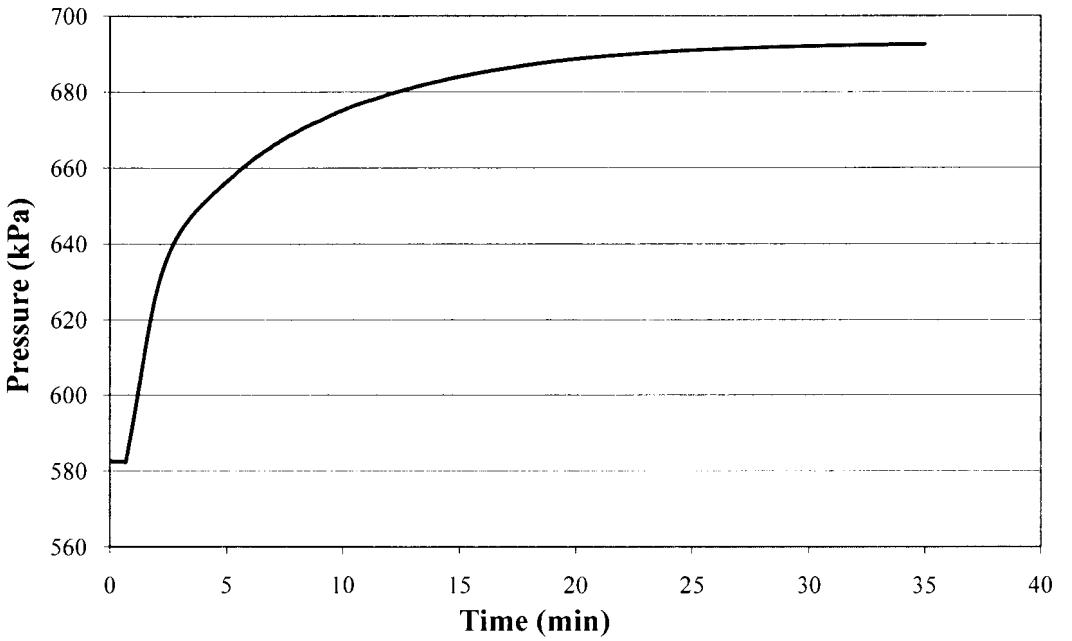

Figure 11. Typical time versus pressure curve.

As can be seen in Figure 11, the pressure is initially constant for a period of time until a spike occurs after several seconds. An initial load is placed on the frame and will remain constant until the foam reaches the top of the mold and creates an additional load, therefore increasing the calculated pressure. The length of dwell time is dependent on both the time the expanding foam takes to reach the top of the mold as well as the amount of time since mixing the two liquids. The time the foam takes to reach the top of the mold is based on the geometry of the mold. A larger mold initially filled with a lesser amount of liquid would lead to a longer dwell time before an increase in pressure is seen. This length of time may also be dependent on the amount of time between the initial mixing of the two

liquids and their injection into the mold. The mixing of the liquids for this research was done by hand and took an average of 20 seconds to complete. For a larger scale panel, such as those produced at SAS, the liquids are mixed and dispensed with a mixing head, which takes only seconds to complete. The difference in these mixing times and methods may play a role in the measured time of the completed reaction. The mixing method may also play a role in the polymerization reaction due to how well the two liquids were combined. The results from each of the foaming trials are shown below in Table 2.

Table 2. Foaming results from Frame A.

Preload	Pressure, initial	Pressure, final	Density	Flash	Weight
kN	(MPa)	(MPa)	g/cm^3	grams	grams
10	3.53	.997	0.387	1.0	50.6
8	2.87	.835	0.427	1.9	55.9
6	2.15	.666	0.436	4.4	57.0
6 (2nd)	2.16	.673	0.433	4.3	56.7
6 (3rd)	2.13	.690	0.407	4.4	53.3
5	1.71	.552	0.430	4.0	56.3
3.5	1.21	.407	0.384	2.9	50.2

In order to more closely examine the trends in these results a plot of the flash versus pressure was constructed and is shown in Figure 12. Generally, when the amount of flash was reduced, the pressure was found to increase. This trend can be seen by the linear trend line, which has a negative slope. With a larger amount of material contained inside the mold the pressure increase was expected.

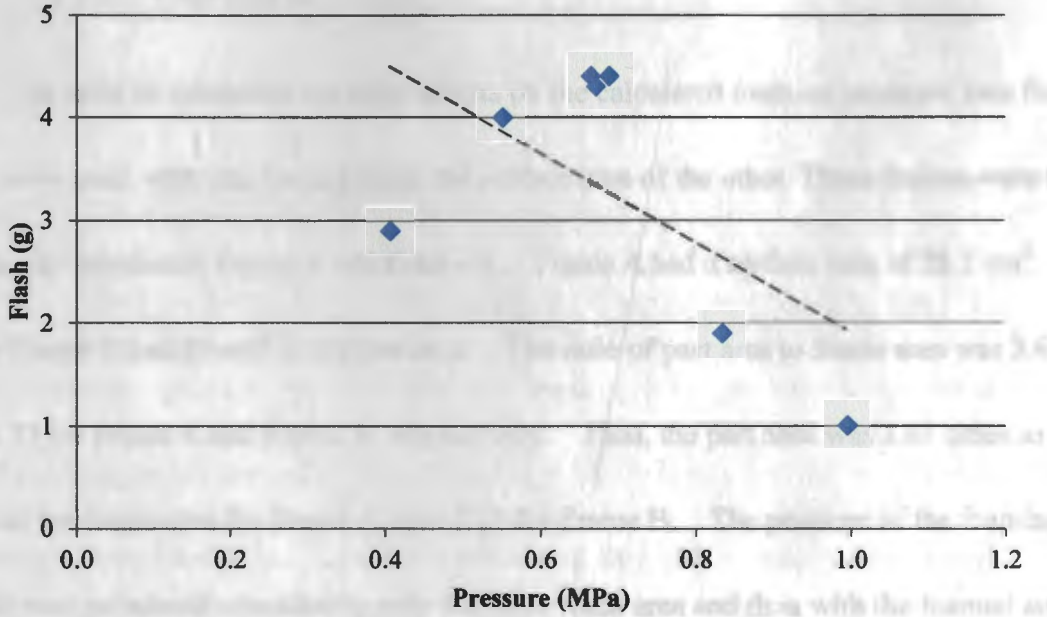

Figure 12. Flash versus pressure.

4.1.1.2. Frame C

Frame C was tested with a much larger preload, due to the increase in area. A preload of 133 kN was used, which correlates to an initial pressure of 3.04 MPa on the frame. This value was chosen to correspond with the initial pressures used on Frame A. A final average load of 149.5 kN was generated, correlating to a final pressure of 0.896 MPa. The pressure generated was 8.6% larger than that found when using Frame A and had a density in the same range. This shows that there may be an effect of scaling up the experiment due to the use of a larger volume of material.

4.1.1.3. Edge Effects

In order to determine the edge effects on the calculated foaming pressure, two frame sizes were used, with one having twice the surface area of the other. These frames were the previously mentioned Frame A and Frame B. Frame A had a surface area of 28.2 cm^2, while Frame B had 60 cm^2 of surface area. The ratio of part area to frame area was 3.67 and 1.71 for Frame A and Frame B, respectively. Thus, the part area was 3.67 times as large as the frame area for Frame A, and 1.71 for Frame B. The pressure of the foaming liquids was calculated considering only the inner foam area and then with the foamed area plus the frame area. These pressures were calculated and compared for each of the two frames. The percentage difference between these two values were found to be 21.4% for Frame A and 36.9% for Frame B. With these values varying significantly, it was determined that the size of the frame played a role in the pressure calculated using this method. However, the pressure calculated when ignoring the frame and using only the part area was the same for each of the frames. This shows that towards the end of the foaming reaction the foaming polyurethane supports all of the load and the frame does not have any load acting on it. Therefore, when calculating the pressure values, the size of the frame was neglected and only the part area was used. The molds used for making a larger scale product at SpaceAge Synthetics Inc. need to be strong enough to contain the expanding foam and the pressure applied to the top of the mold needs to be greater than the

pressure generated in the foam in order to ensure the mold will remain shut during expansion.

4.1.1.4. Verification of Results

To ensure the pressure generated during the foaming process fell within the assumed range, a pressure sensitive paper was used. The paper deepens in color as the pressure increases and measures in the range of 0.482 MPa and 2.41 MPa. To determine the pressure generated in the foam, the load created during the foaming process was divided by the area in contact with the load frame, in this case the foamed area in addition to the frame area. The pressure sensitive paper was laid up inside the mold before the liquids were injected and left in place throughout the experiment. The calculated pressures were near the low end of the pressure range capable of being measured with the paper, which gave a faint color change, thus indicating that the calculated pressures were in the correct range. The initial pressure on the frame due to the preload was 3 MPa, which is larger than the maximum value achievable by the pressure sensitive paper, thus turning the paper to the darkest possible color. The dark square is a result of the initial pressure and the lighter interior is the area in which the foaming reaction took place. The results from this test are shown below in Figure 13.

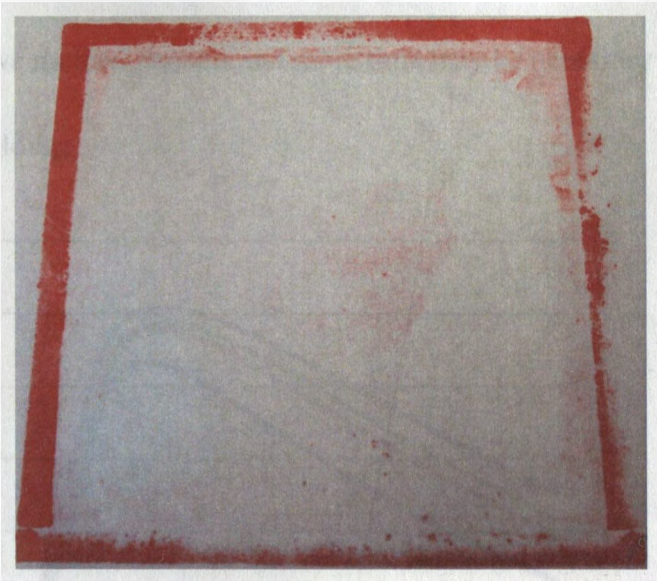

Figure 13. Pressure paper results.

4.1.2. Temperature Profile

The resulting temperature profiles found at varying heights inside a foaming sample are shown in Figure 14. Since polyurethane foam is a good insulator, the thermocouples in the center of the foam exhibited larger maximum temperatures, while those along the bottom surface did not rise as high. It can be seen that the top-center thermocouple exhibited a delay in the temperature rise while those on the bottom of the cup exhibited an instant change. The top-center thermocouple was initially placed above the liquid level, therefore not coming into contact with the reacting material until the reaction was already taking place. As can be seen from the experiment, the exotherm produced during the reaction did not reach 150 °C, which is later shown to be within the safe working temperature of both of the liquids. With such an increase in temperature, the molds may

retain heat for successive molded pannels and more time may be necessary for the material to solidify before demolding.

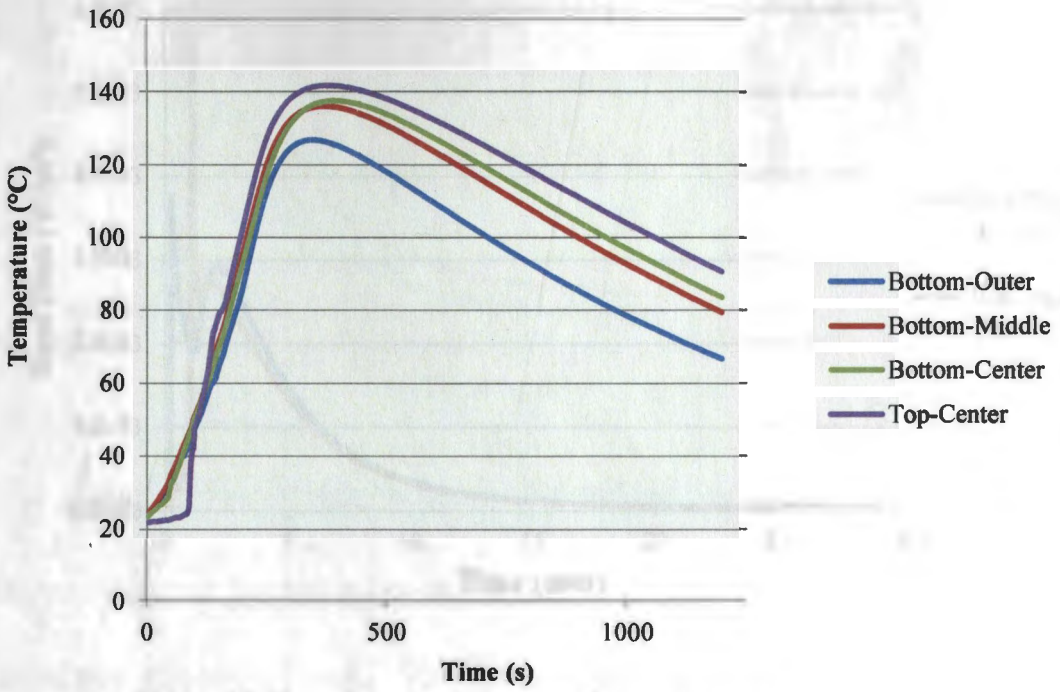

Figure 14. Thermal profile during foaming reaction.

4.1.3. Heat Flux

Heat flux measurements were taken at the interface between the foaming liquid and the top or bottom plates. The molds used at SAS to produce the Thermo-Lite composite consist of two different materials, steel and a wood MDF board. Depending on the machine in which the boards are processed the bottom plate is either steel or MDF, while

the top plate is always steel. The heat flux results are shown in Figure 15 for the case of two steel plates and one steel and one MDF plate.

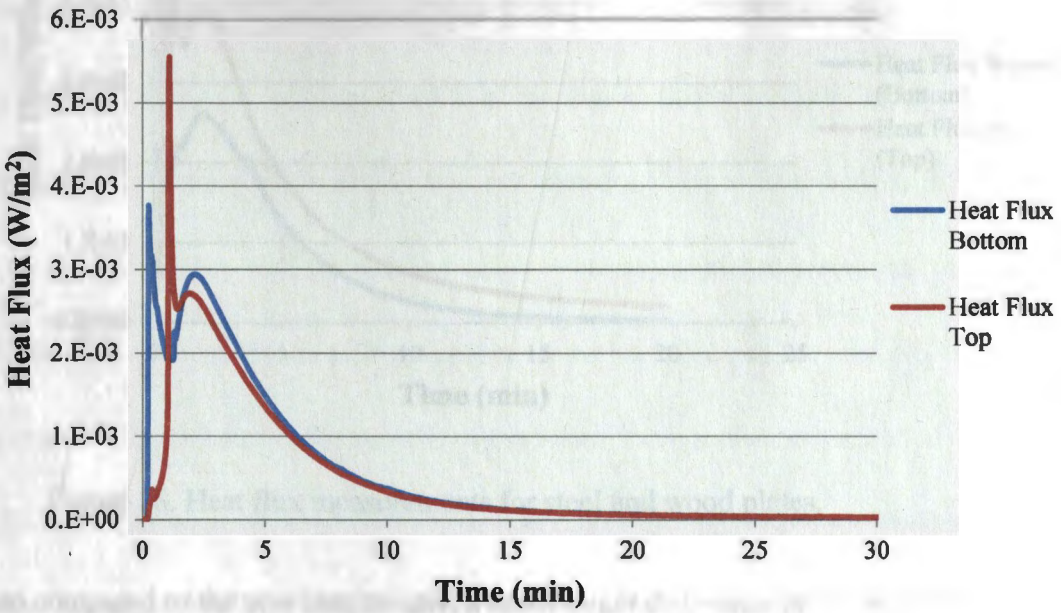

Figure 15. Heat flux measurements for steel plates.

With both plates being made of the same material the heat flux through the sensor at the interface was found to be roughly the same value. However, when changing the bottom plate to a MDF wood material, the heat flux through the interface was found to differ significantly from that of the steel. Wood is a better insulator, therefore decreasing the amount of heat flux out of the foam along the bottom of the panel. The heat flux results for the case of a steel top and a MDF wood bottom are shown below in Figure 16.

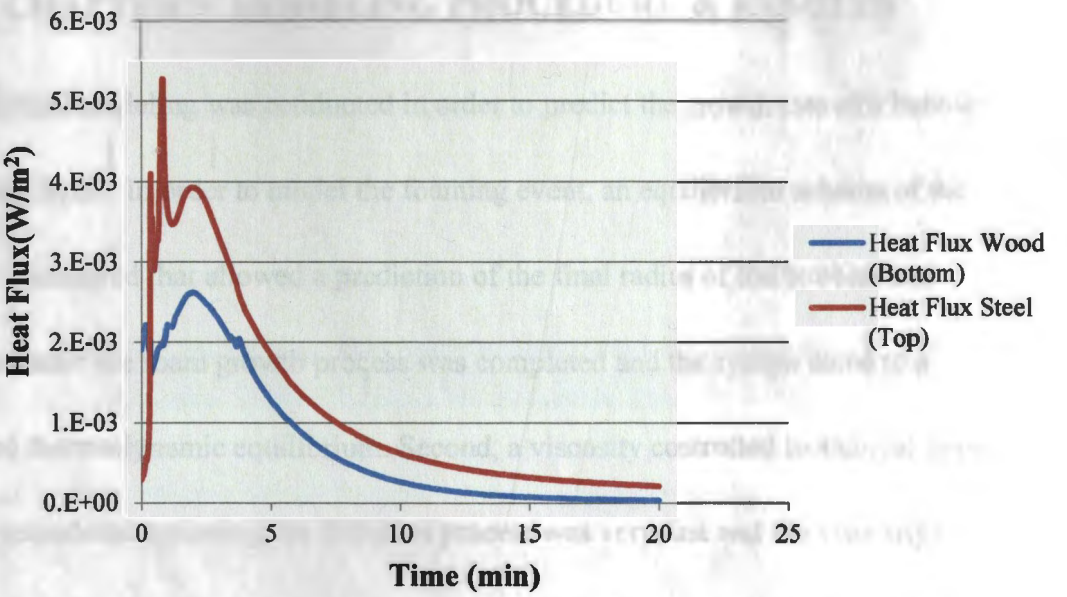

Figure 16. Heat flux measurements for steel and wood plates.

When compared to the previous sample, a much larger difference in the heat flux is seen due to the varying materials used. With metal being such a good thermal conductor, a larger heat flux is seen at the foam/steel interface than between the foam and the wood. Having a large difference in the thermal conductivity of the mold surfaces may cause panel warpage due to changes in the thermal profile throughout the thickness. A material with a low thermal conductivity will contain the heat at the interface rather than letting it dissipate, making for a higher temperature for a longer duration.

CHAPTER 5. MODELING PROCEDURE & RESULTS

Analytical modeling was conducted in order to predict the growth rate of a bubble in the foaming liquid. In order to model the foaming event, an equilibrium scheme of the process was considered that allowed a prediction of the final radius of the bubbles and foam pressure after the foam growth process was completed and the system came to a mechanic and thermodynamic equilibrium. Second, a viscosity controlled isothermal foam growth was considered assuming the diffusion process was very fast and the viscosity of the liquid was the limiting factor to the growth of the foam. Then, diffusion controlled isothermal foam growth was considered assuming that liquid viscosity was very small and the diffusion of gas into the cell was what limited the growth of the foam. The liquid polymerization kinetics were discussed and a mathematical algorithm of how to identify the parameters of the model were shown. Finally, the heat transfer process through the foam accompanied with the heat released due to polymerization is discussed as the direction of future research. In order to create a simplified model of the foaming process, some assumptions were made in order to examine each phenomena individually before combining them to examine the process as a whole.

The assumptions made for the experimental modeling are summarized and the equations used in modeling the foam growth are given in the following sections.

Mathematical models of differing levels of complexity are presented to model the experimental set-up of the foaming liquid, which is seen in Figure 17.

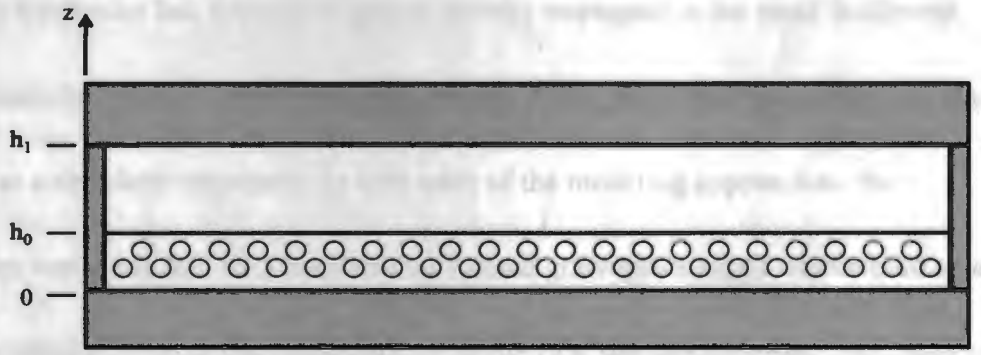

Figure 17. Modeling set-up.

Similar to the experimental setup, a mixture of liquid compounds, which contains a foaming agent and is able to polymerize, is examined. The liquid is taken as having an initial height of h_o. The foaming agent reacts with the liquid polyol producing a gas, making the liquid oversaturated with carbon dioxide gas. Due to heterogeneous nucleation, bubbles start to form and subsequently grow, causing a swelling of the liquid in the z-direction. The liquid surface rises until it reaches the cover placed on top of the case at a height of h_1. After that point, the volume of the mixture does not change, but the polymerization reaction accompanied with heat release continues. When the polymerization reaction is completed, the heat exchange with the surroundings brings the system back to room temperature.

5.1.Assumptions

5.1.1. Equilibrium Scheme

The initial modeling assumed atmospheric conditions since during manufacture at SpaceAge Synthetics Inc. venting of gasses initially entrapped in the mold is allowed through machined vents. A constant temperature during the foaming reaction was also assumed as a simplistic approach. As with each of the modeling approaches, the assumption was made that each nucleus that formed grew into a single, stable bubble, and that upon initial mixing of the two liquids all of the CO_2 gas was generated and dissolved in the liquids instantaneously. The liquid dimension in the plane of the substrate is much larger than its thickness and lateral effects are negligible so that the primary bubble growth may be considered essentially one-dimensional, with growth occurring in the z-direction (perpendicular to the substrate). A uniform temperature across the cell is assumed, such that all bubbles and cells associated with them have equal size.

5.1.2. Liquid Viscosity Controlled Bubble Growth

Similarly, the assumption was made that each nucleus that formed grew into a single, stable bubble and that the primary bubble growth occurs in the z-direction. In this phase, the viscosity of the liquid was assumed to be the factor that inhibited the rate of the growth of the bubble and the diffusion of the gas through the liquid is taken as infinitely

fast. The initial conditions were taken at room temperature and atmospheric pressure for each of the variables used. The gas bubble and foam cell were assumed spherical and concentric.

5.1.3. Diffusion Controlled Bubble Growth

The same assumptions were made that each nucleus that formed grew into a single, stable bubble and that the primary bubble growth occurs in the z-direction. In this phase, the diffusion of gas through the liquid was assumed to be the factor that inhibited the rate of the growth of the bubble and the viscosity of the liquid is taken as infinitely small. Again, the initial conditions were taken at room temperature and atmospheric pressure for each of the variables used, and the gas bubble and foam cell were assumed spherical and concentric.

5.1.4. Glass Loading

The SpaceAge Synthetics Inc. Thermo-Lite composite board contains varying architectures of glass loading, while the experimental work contained only foam. A burn off test was conducted to determine the volume fraction of glass in the composite by heating the sample to a temperature high enough to degrade the polyurethane while leaving the glass intact. It was found that a 5.08 cm thick, 0.48 g/cm^3 board containing filter material and continuous fiber mat contained only 2.11% glass by volume. This small volume of

glass was assumed to have little impact on the foaming reaction of the polyurethane. An examination of the cellular structure was also conducted on several composite boards under a microscope. It was seen that several complete cells existed between adjacent glass fibers, lending to the belief that the glass reinforcement does not impede the growth of the bubbles. This can be seen below in Figure 18 with the glass fiber seen as the straight lines and the foam pores having a circular geometry.

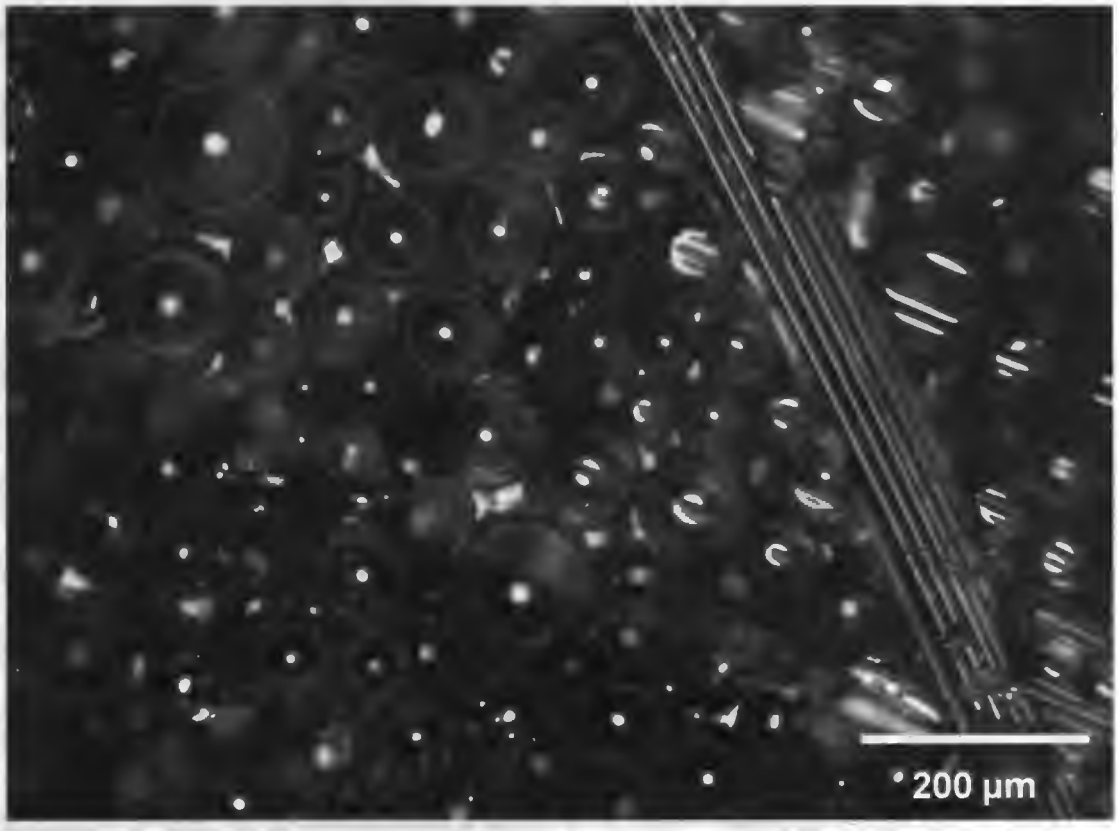

Figure 18. Several complete cells between adjacent glass fibers.

5.1.5. Sphere Impingement

The simplification of each of the models presented is concerned with only one cell growing in the liquid. An amount of liquid was divided into several cells, with each cell being taken as an average spherical bubble growing in the liquid. Each cell was examined individually without exploring the interference caused by neighboring bubbles. In reality, neighboring bubbles caused impingement that led to final bubbles that were not completely spherical. With bubbles in contact with each other, there is a sharing of liquid in the adjoining cell wall that is not taken into consideration in the modeling presented in this work. This interference with other bubbles in the foam may be of further interest in a more complex foaming model.

5.2. Modeling Setup & Results

5.2.1. Equilibrium Scheme

A liquid layer of thickness h_0 on a plane substrate is considered, as shown in Figure 17. The liquid initially contains some amount of dissolved gas, which was generated due to the chemical reaction between the isocyanate and the foaming agent. The concentration of the gas is measured in kg of gas per kg of liquid and is equal to c_0, which is larger than the concentration of this gas dissolved in this liquid at normal conditions (equal to c_s). Thus, the liquid is initially oversaturated with gas.

The number of gas bubble nuclei per unit mass of liquid is given as n_0. The total number of bubble nuclei per unit area of the substrate, N, is

$$N = n_0 \rho_l(T_0) h_0 \tag{1.1}$$

where $\rho_l(T_0)$ is the initial liquid density at room temperature.

According to a cell model, a foaming liquid pool that contains a large number of bubbles can be divided onto many cells [51], with a schematic of the cell presented in Figure 19.

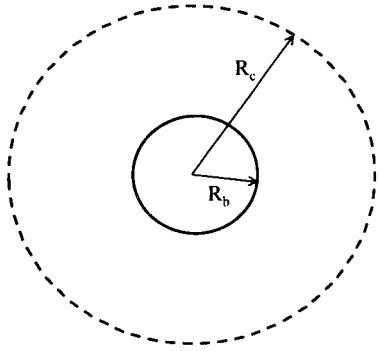

Figure 19. Schematic of a cell in a foaming liquid.

Each individual cell contains a single bubble and a specific amount of liquid, m_l calculated as

$$m_l = \frac{4}{3}\pi\left(R_c^3 - R_b^3\right)\rho_l(T) = \frac{1}{n_0} \tag{1.2}$$

Here R_c, R_b are radius of the cell and radius of the bubble in this cell, and $\rho_l(T)$ is the liquid density at the current temperature. The temperature is assumed to be uniform across the cell and the foam layer, such that all bubbles and cells associated with them have equal size.

After the liquid starts foaming the bubble radius and the cell radius increase such that at some moment the foaming liquid reaches the upper cover that is placed at a distance h_l from the substrate. At this moment, R_c is calculated from the equation

$$\frac{4}{3}\pi R_c^3 N = h_l \tag{1.3}$$

and after this point R_c will stay constant. The bubble radius after the foaming liquid has reached the cover can be calculated using the Equations (1.1) - (1.3) as follows

$$\frac{4}{3}\pi R_b^3 = \frac{1}{n_0\rho_l(T_0)}\left[\frac{h_l}{h_0} - \frac{\rho_l(T_0)}{\rho_l(T)}\right] \tag{1.4}$$

This equation shows that, in general, after the moment in which the foam reaches the lid, according to this equation, the bubble radius R_b may change with temperature.

Mechanical equilibrium of the bubble is reached if the equation

$$p_f = p_g - \frac{2\sigma}{R_b} \tag{1.5}$$

is satisfied. Where σ is the liquid surface tension coefficient, p_f is the foam pressure, and p_g is the gas pressure in the bubble, which is calculated according to the ideal gas law

$$p_g = \frac{m_g}{\frac{4}{3}\pi R_b^3} R_g T \tag{1.6}$$

Here m_g is mass of the gas in the bubble and R_g is the gas constant for the foaming gas. Combining the Equations (1.5) and (1.6) the following equilibrium condition was obtained

$$p_f = \frac{m_g}{\frac{4}{3}\pi R_b^3} R_g T - \frac{2\sigma}{R_b} \tag{1.7}$$

The gas mass balance in a cell at the diffusion equilibrium condition can be formulated in the following form

$$m_l c_0 = m_g + m_l c \tag{1.8}$$

where c is an equilibrium gas concentration dissolved in the liquid in the cell, which is calculated with Henry's law,

$$c = Hp_g \tag{1.9}$$

where H is Henry's Law constant. Combining the Equations (1.6), (1.8), and (1.9) one can derive the following equation for the mass of gas in the bubble

$$m_g = \frac{m_l c_0}{1 + \dfrac{m_l H R_g T}{\dfrac{4}{3}\pi R_b^3}} \tag{1.10}$$

The Equations (1.4), (1.7) and (1.10) are the set of equations to calculate R_b, m_g, and p_f when foaming liquid has reached the cover, if h_l/h_0, T/T_0 are known along with all necessary thermodynamic parameters of the foaming liquid. It is convenient to present the Equations (1.4), (1.7) and (1.10) in dimensionless form:

$$\overline{R}_b = \left[\frac{h_1}{h_0} - \frac{\rho_l(T_0)}{\rho_l(T)} \right]^{1/3} \tag{1.11}$$

$$\overline{m}_g = \left[1 + c_s \overline{\rho}_l(T_0) \frac{T}{T_0} \frac{1}{\overline{R}_b^3} \right]^{-1} \tag{1.12}$$

$$\bar{p}_f = c_0 \bar{\rho}_l(T_0) \frac{T}{T_0} \frac{\bar{m}_g}{\bar{R}_b^3} - \frac{2\bar{\sigma}}{\bar{R}_b} \tag{1.13}$$

Here the unknown variables R_b, m_g, and p_f are normalized as

$$\bar{R}_b = \frac{R_b}{R_0}, \quad \bar{m}_g = \frac{m_g}{m_l c_0}, \quad \bar{p}_f = \frac{p_f}{p_{atm}} \tag{1.14}$$

The following parameters were also used when normalizing Equations (1.4), (1.7), and (1.10):

$$\begin{aligned} &m_l = \frac{1}{n_0}, \quad R_0 = \left[\frac{3}{4\pi n_0 \rho_l(T_0)} \right]^{1/3}, \quad p_{atm} = \rho_{g*} R_g T_0, \\ &c_s = H p_{atm}, \quad \bar{\rho}_l(T_0) = \frac{\rho_l(T_0)}{\rho_{g*}}, \quad \bar{\sigma} = \frac{\sigma}{R_0 p_{atm}} \end{aligned} \tag{1.15}$$

Here R_0 is the radius of a cell at room temperature, when a bubble nuclei has not yet been generated, ρ_{g*} is the gas density at room temperature and atmospheric pressure.

5.2.1.1. Determination of Values

In order to model the foaming reaction, several material property values needed to be evaluated. The determination of the initial bubble radius, number of nuclei, surface tension, and diffusion coefficient are shown below.

Initial Bubble Radius

The initial size of the bubble in the liquid was unable to be measured during the foaming reaction so a measurement of the final bubble size was taken and the initial bubble size was predicted from that value. The equilibrium modeling for the initial and final heights of the liquid was completed and the normalized radius of the bubble ($\overline{R}_b$) was found to be 1.45 for the modeling parameters used. A microscope with a computer imaging system was used and an average final bubble radius of 107 μm was found for the experimental setup used. A picture of a cross section of 0.256 g/cm^3 density foam is shown in Figure 20 with the bubble diameter shown for each of the cells measured in the viewing area.

Table 3 shows the average measured bubble size for two foam densities and two thicknesses of the PU foam. The average bubble radius was found to decrease with increasing foam density. When adding a larger amount of liquid into the mold an increased density will result and smaller bubbles will be created in the foam.

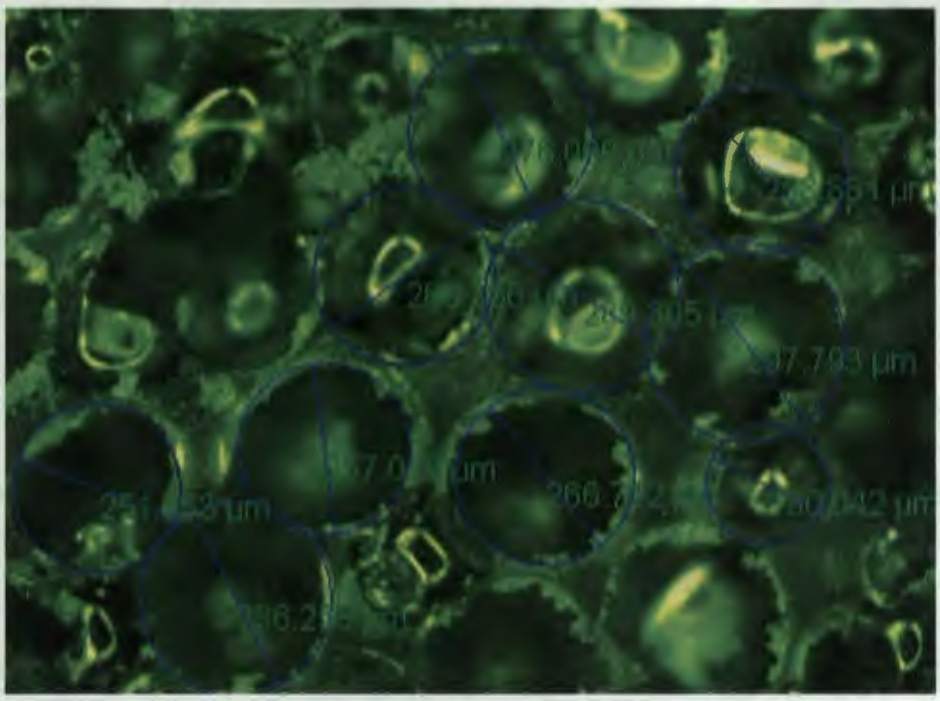

Figure 20. Measurement of bubble diameters in polyurethane foam.

Table 3. Cell size measurements.

Target Thickness (mm)	Target Density (g/cm^3)	Average Radius (μm)	Standard Deviation (μm)
12.7	0.240	186	37.8
25.4	0.240	217	52.6
12.7	0.481	152	36.0

The equation for the radius of the bubble is

$$\overline{R}_b = \frac{R_b}{R_0} \tag{1.16}$$

making the initial bubble radius equal to 73.8 μm.

Number of Nuclei

The number of nuclei per unit mass of liquid at normal conditions, or n_0, is calculated as

$$n_o = \frac{3}{4\pi\rho_l(T_o)R_o^3} \tag{1.17}$$

with R_o being calculated as stated above and $\rho_l(T_o)$ being the liquid density at standard conditions. The number of nuclei was found to be 576,600,000 nuclei per kilogram of liquid.

Surface Tension

The surface tension of each of the liquids was measured using the pendant drop method. The average of the two values was used in the modeling since the two liquids were mixed in equal proportions by volume. The surface tension of the isocyanate and polyol mixture was found to be 0.03 N/m.

Diffusion Coefficient

The ability of a gas to diffuse through a liquid is given by a diffusion coefficient. This coefficient was found to be between $0.5 \times 10^{-9} - 5 \times 10^{-9}$ m^2/s for liquids [60]. A value in the middle of this range was chosen for use in the model, or 2.5×10^{-9} m^2/s. The

diffusion coefficient for the range given was not shown to have a large effect on the final bubble radius or foam pressure. The value of the diffusion coefficient will, however, play a role in the time it takes the bubble to reach its final size and pressure.

5.2.1.2. Equilibrium Scheme Results

The pressure in the foam, mass of gas in the bubbles, and radius as a function of the initial height to the final height were determined and shown in Figures 21-23 below for four different temperatures (held constant throughout the entire foaming reaction).

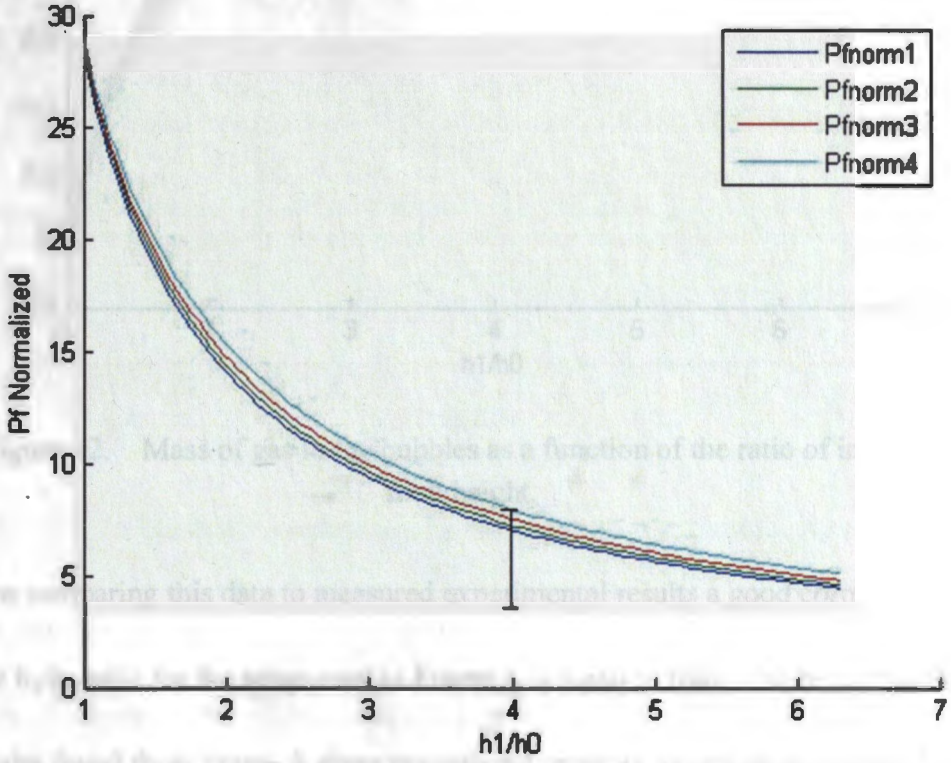

Figure 21. Foam pressure as a function of initial to final height ratio.

The four temperatures used for this modeling were 26°C, 37°C, 52°C, and 77°C (1, 2, 3, 4). Each of the temperature values were normalized with respect to initial conditions, or 21°C. Again, the pressure was normalized with respect to atmospheric pressure, or 101.3 kPa.

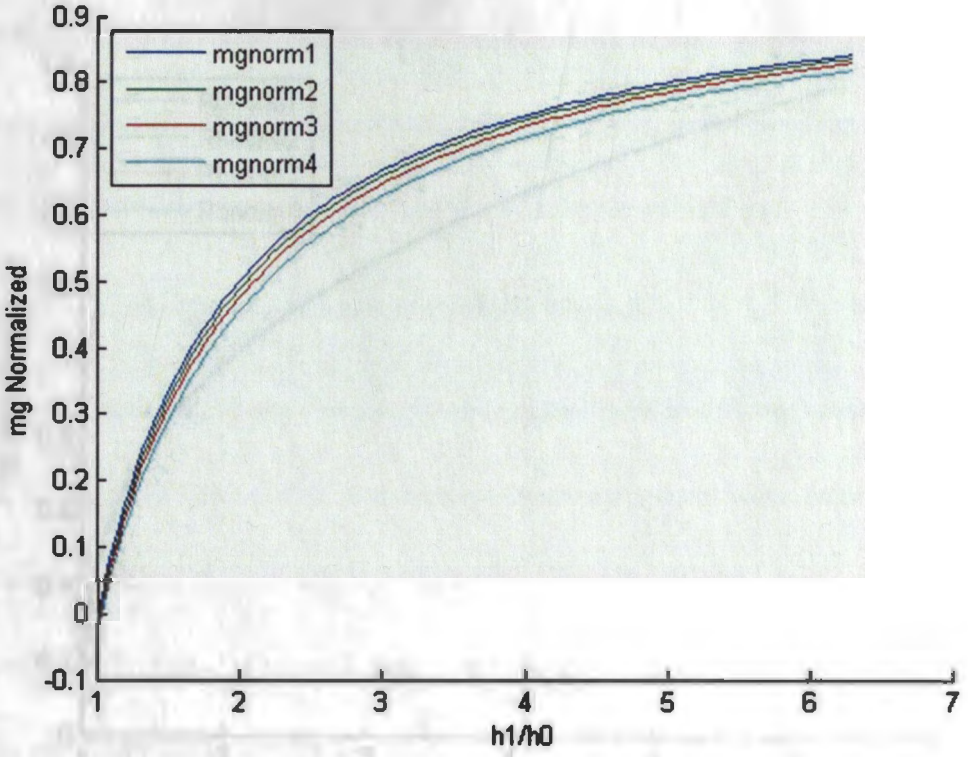

Figure 22. Mass of gas in the bubbles as a function of the ratio of initial to final height.

When comparing this data to measured experimental results a good correlation exists. The h_1/h_0 ratio for the setup used in Frame A is equal to four. Normalizing the pressure results found from Frame A gives normalized pressure values ranging from 7.73 to 3.15. At the highest value it falls within the four lines plotted in Figure 21, and at the lowest

it falls slightly below the curves. The model presented is an ideal scenario assuming all material placed inside the mold remains inside and will aide in the creation of pressure. In reality, some material escapes from the mold, making the pressure generated lesser than the ideal case.

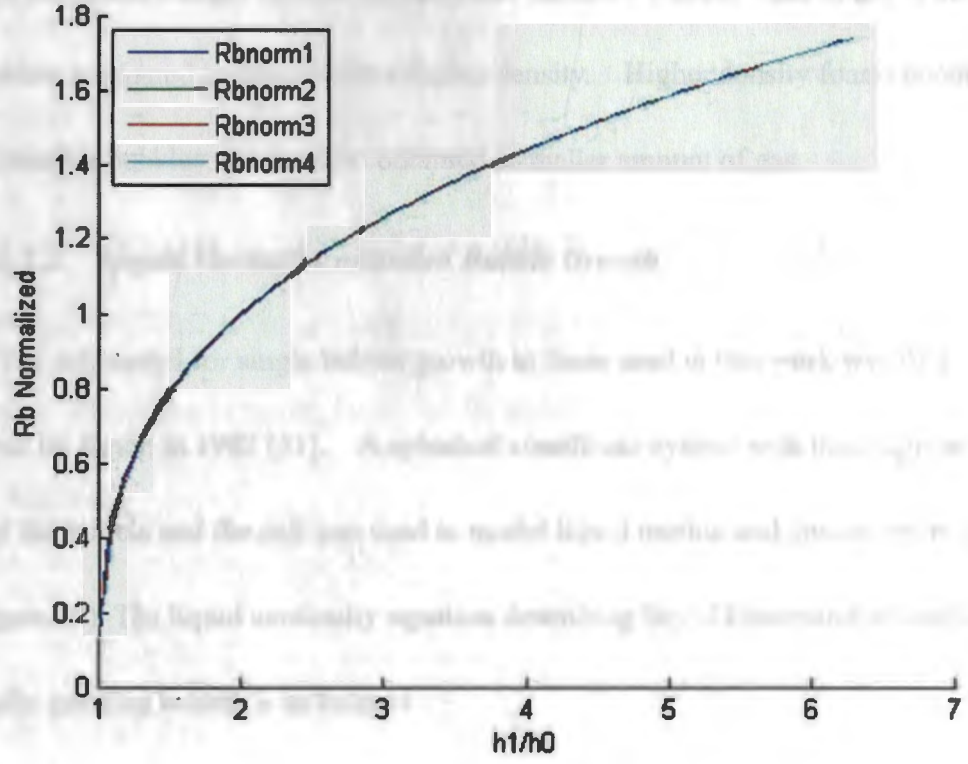

Figure 23. Final bubble radius as a function of initial to final height ratio.

As it can be seen, the mass of the gas and the pressure in the foam are more dependent on temperature than is the final radius of the bubble. The ratio of initial to final height of the foam is increasing from left to right in the previous figures. A larger ratio

would represent a smaller amount of material placed into a large mold, a smaller ratio being the opposite. Therefore, a large ratio would allow for greater expansion of the foam and result in a lesser foam pressure, bigger bubbles, and a larger mass of gas in each bubble when compared to a smaller ratio. As was shown in Table 3, the foam with a lesser density (or larger ratio) had a larger bubble diameter and therefore a larger mass of gas in each bubble when compared to foams with a higher density. Higher density foams contained several, smaller bubbles which each contained a smaller amount of gas.

5.2.2. Liquid Viscosity Controlled Bubble Growth

The cell model for single bubble growth in foam used in this work was first developed by Amon in 1982 [51]. A spherical coordinate system with the origin in the center of the bubble and the cell was used to model liquid motion and gas transport in the cell (Figure 19). The liquid continuity equation describing liquid kinematics around a spherically growing bubble is as follows

$$\frac{1}{\rho_l}\frac{d\rho_l}{dt}+\frac{1}{r^2}\frac{\partial}{\partial r}\left(r^2 u_l\right)=0, \quad \frac{d}{dt}=\frac{\partial}{\partial t}+u_l\frac{\partial}{\partial r} \tag{2.1}$$

where r is the radial coordinate, $u_l(r,t)$ is the radial liquid velocity, and d/dt is a material derivative. The liquid velocity on the bubble/liquid interface is equal to the radial

velocity of the bubble wall

$$u_l\big|_{r=R_b} = \dot{R}_b, \quad \dot{R}_b = \frac{dR_b}{dt} \tag{2.2}$$

In most cases it can be assumed that liquid density in the cell is uniform and time dependant, $\rho_l=\rho_l(t)$. It may change in time due to changing foam temperature and pressure, which are considered uniform across the cell. The Equation (2.1) after multiplication by r^2 can be integrated over the radial coordinate from the bubble/liquid interface, R_b, to some arbitrary radius r. Using boundary condition (Equation (2.2)), the following relation between the radial liquid velocity field, bubble radius change, and liquid density change, can be obtained:

$$u_l = \frac{R_b^2 \dot{R}_b}{r^2} - \frac{1}{3}\frac{d\ln\rho_l}{dt}\left(r - \frac{R_b^3}{r^2}\right) \tag{2.3}$$

The liquid dynamics around a spherically growing bubble are described by the Navier-Stokes equation in the following form:

$$\rho_l\left(\frac{\partial u_l}{\partial t}+u_l\frac{\partial u_l}{\partial r}\right)=-\frac{\partial p_l}{\partial r}+\mu\left[\frac{1}{r^2}\frac{\partial}{\partial r}\left(r^2\frac{\partial u_l}{\partial r}\right)-\frac{2u_l}{r^2}\right] \tag{2.4}$$

This equation represents a balance between the liquid inertia forces (left side), pressure gradient, and liquid viscosity forces (second term of right side). It can be seen, that for the velocity field, Equation (2.3), the viscous term in the Equation (2.4) is equal to zero. In the case of foam bubble growth the inertia forces can be neglected, since the bubble growth happens relatively slowly (in comparison with liquid speed of sound). Thus, $\partial p_l / \partial r \cong 0$ and the liquid pressure can be considered uniform, but time dependent, $p_l = p_l(t)$.

The radial component of stress changes with the radius due to the viscous stresses as follows

$$\sigma_{rr}=-p_l+2\mu\frac{\partial u_l}{\partial r} \tag{2.5}$$

Then the boundary conditions representing the force balance at the bubble/liquid interface and cell boundary are written as follows

$$\begin{aligned} p_g &= p_l-2\mu\frac{\partial u_l}{\partial r}+\frac{2\sigma}{R_b}, && r=R_b \\ p_f &= p_l-2\mu\frac{\partial u_l}{\partial r}, && r=R_c \end{aligned} \tag{2.6}$$

where p_g, p_f are gas pressure in the bubble, and pressure in the foam. Using these equations to eliminate the liquid pressure the equation becomes

$$p_g - p_f = -2\mu \left.\frac{\partial u_l}{\partial r}\right|_{r=R_b} + 2\mu \left.\frac{\partial u_l}{\partial r}\right|_{r=Rc} + \frac{2\sigma}{R_b}, \tag{2.7}$$

Substituting the velocity field (Equation (2.3)) into this equation gives the following equation for the radius of the bubble

$$p_g - p_f = 4\mu\left(\frac{\dot{R}_b}{R_b} + \frac{1}{3}\frac{d\ln\rho_l}{dt}\right)\frac{R_c^3 - R_b^3}{R_c^3} + \frac{2\sigma}{R_b} \tag{2.8}$$

Introducing the liquid mass in the cell (Equation(1.2)) the Equation (2.8) can be rewritten in the following form:

$$\dot{R}_b = \frac{R_b}{4\mu}\frac{\frac{3m_l}{4\pi\rho_l(T)} + R_b^3}{\frac{3m_l}{4\pi\rho_l(T)}}\left(p_g - p_f - \frac{2\sigma}{R_b}\right) - \frac{R_b}{3}\frac{d\ln\rho_l(T)}{dt} \tag{2.9}$$

Using Equations (1.14), (1.15) the Equation (2.9) can be presented in the following dimensionless form:

$$\frac{d\bar{R}_b}{d\bar{t}} = \bar{R}_b\left(1+\frac{\rho_l(T)}{\rho_l(T_0)}\bar{R}_b^3\right)\left(\bar{p}_g-\bar{p}_f-\frac{2\bar{\sigma}}{\bar{R}_b}\right)-\frac{\bar{R}_b}{3}\frac{d\ln\rho_l(T)}{d\bar{t}},\quad \bar{t}=\frac{t}{\tau_\mu},\quad \tau_\mu=\frac{4\mu}{p_{atm}} \tag{2.10}$$

The Equation (2.10) can be used to calculate how bubble radius changes in time if the algorithms for temperature, gas pressure in the bubble, and foam pressure are defined. In an isothermal situation the last term in the Equation (2.10) becomes equal to zero, or

$$\frac{d\bar{R}_b}{d\bar{t}} = \bar{R}_b\left(1+\bar{R}_b^3\right)\left(\bar{p}_g-\bar{p}_f-\frac{2\bar{\sigma}}{\bar{R}_b}\right) \tag{2.11}$$

The foam growth process can be divided into two periods: a free foam growth period and a confined foam growth period. In the free foam growth period, the liquid level is rising ($h<h_l$), and the pressure in the foam is known and equal to atmospheric pressure ($p_f = p_{atm}$). Once the foaming liquid reaches the upper cover ($h=h_l$), the confined foam growth period begins and the pressure in the foam is calculated.

During the free foam growth period the pressure in the foam is equal to atmospheric pressure and the bubble radius changes in time according to the equation

$$\frac{d\overline{R}_b}{d\overline{t}} = \overline{R}_b\left(1+\overline{R}_b^3\right)\left(\overline{p}_g - 1 - \frac{2\overline{\sigma}}{\overline{R}_b}\right) \tag{2.12}$$

where the gas pressure in the bubble is calculated from a combination of the ideal gas equation

$$\overline{p}_g = c_0\overline{\rho}_l(T_0)\frac{\overline{m}_g}{\overline{R}_b^3} \tag{2.13}$$

and the diffusion equilibrium condition

$$\overline{m}_g = \left[1+\frac{c_s\overline{\rho}_l(T_0)}{\overline{R}_b^3}\right]^{-1} \tag{2.14}$$

The Equations (2.13) and (2.14) give the following formula for gas pressure

$$\overline{p}_g\left(\overline{R}_b\right) = \frac{c_0\overline{\rho}_l(T_0)}{c_s\overline{\rho}_l(T_0)+\overline{R}_b^3} \tag{2.15}$$

The gas pressure versus bubble radius is presented in Figure 24 by a solid line. The dashed lines shows $1+2\overline{\sigma}/\overline{R}_b$. Points A and B show minimum bubble radius $\overline{R}_{b1}$ that still can grow, and maximum bubble radius $\overline{R}_{b2}$ at which bubble growth stops naturally if

not confined with upper cover. As can be found from Figure 24, R_{b1} is equal to 2.21 x 10^{-2} μm and R_{b2} is 219.9 μm.

A radius versus time curve is presented in Figure 25 for the case of free rise expansion of the foam. The confined foam growth period begins when radius of the bubble has reached the value

$$\overline{R}_b = \left(\frac{h_1}{h_0} - 1\right)^{1/3} \tag{2.16}$$

or the moment in which the foam reaches a height of h_1.

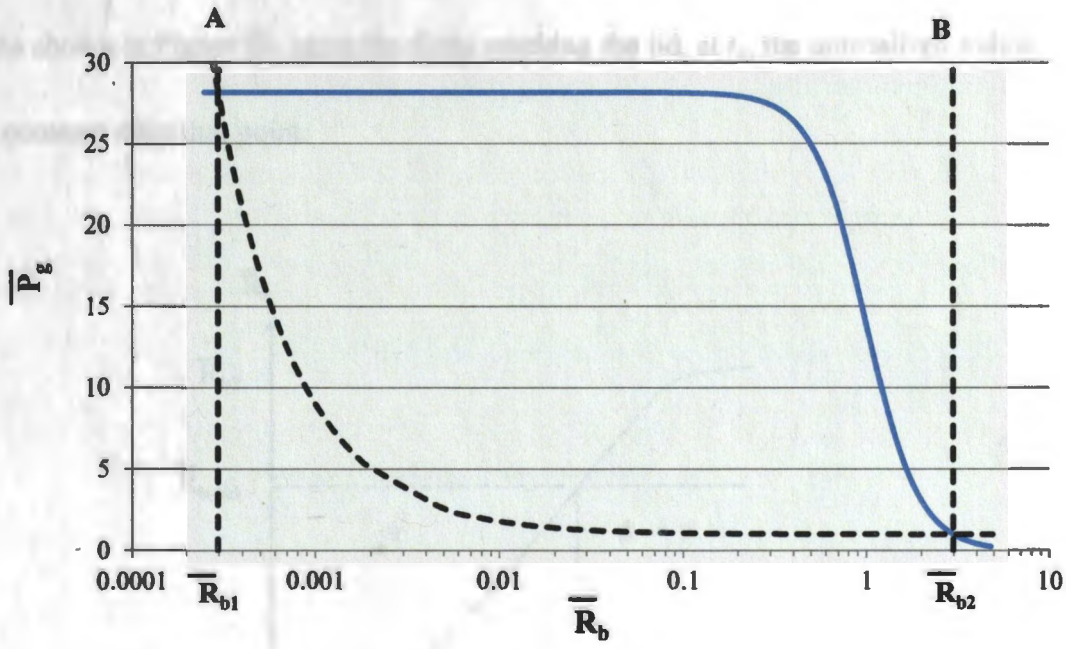

Figure 24. Gas pressure versus bubble radius.

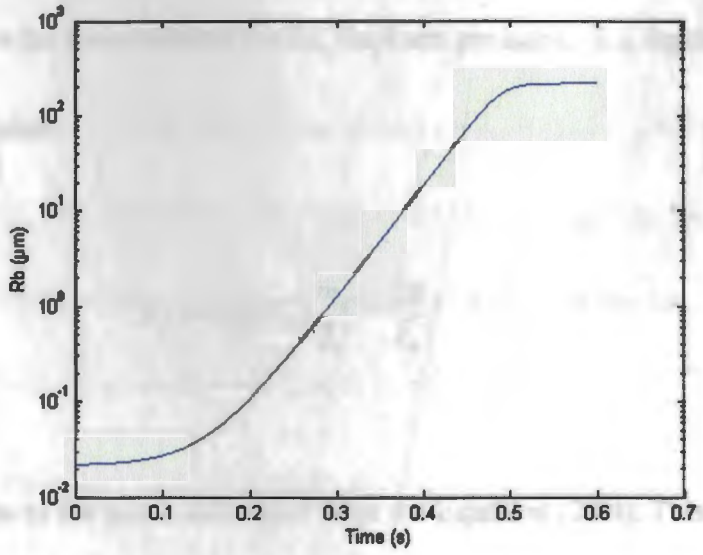

Figure 25. Radius versus time curve for viscosity controlled bubble growth.

As shown in Figure 26, upon the foam reaching the lid, at t_1, the normalized radius remains constant after that point.

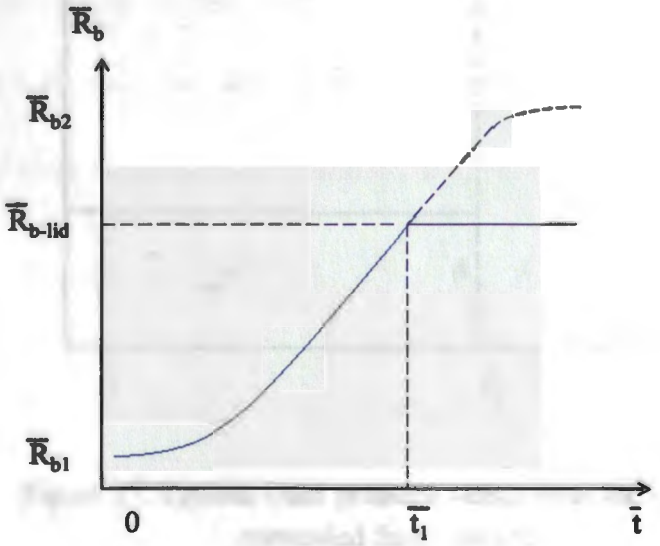

Figure 26. Schematic of bubble size with constrained growth.

At the moment the foam reaches the lid, the foam pressure, $\overline{p}_f$ immediately jumps from 1 to the value

$$\overline{p}_f = c_0 \overline{\rho}_l(T_0) \frac{\overline{m}_g}{\overline{R}_b^3} - \frac{2\overline{\sigma}}{\overline{R}_b} \tag{2.17}$$

where the mass of the gas is calculated from the Equation (2.14). This is shown below in Figure 27.

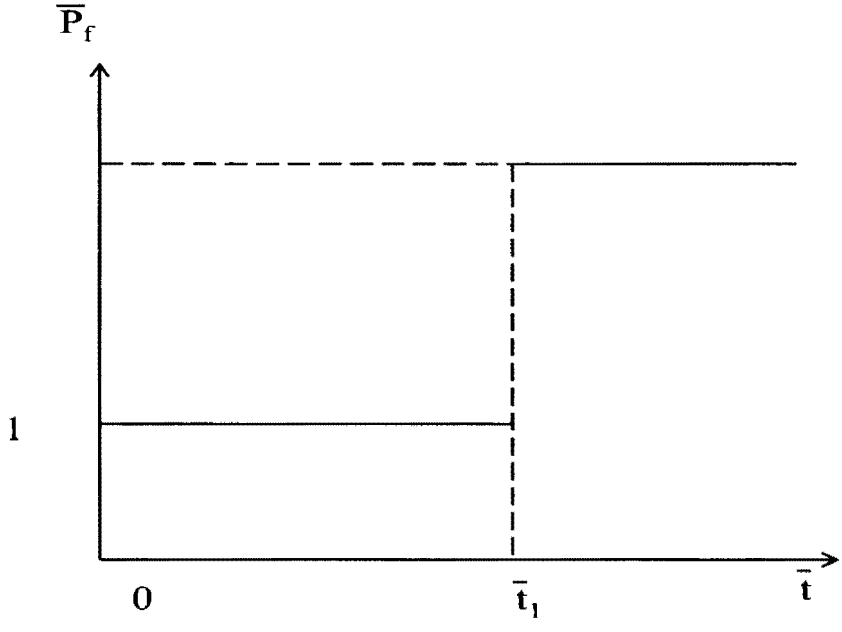

Figure 27. Typical foam pressure versus time for viscosity controlled foam growth.

According to this model, the entire bubble growth occurs in less than a second, which is much quicker than is seen in the experimental work. This shows that the viscosity of the liquid during the foaming reaction is not the limiting factor to the growth of the foam. In applications where the polyurethane is formulated to react at times of less than a second, this model would be a closer prediction than in the case of this research.

5.2.3. Gas Diffusion Controlled Bubble Growth

A setup similar to the viscosity controlled bubble growth was assumed for this phase of the modeling. A spherical coordinated system having the origin in the center of the bubble and the cell was used to model the liquid motion and gas transport in the cell (Figure 19). In this section, the bubble size was calculated for a bubble in mechanical and diffusional equilibrium while the pressure in the liquid is equal to atmospheric pressure (the expanding foam did not yet reach the cover of the mold). The gas mass balance in a cell at diffusion equilibrium was formulated in the following form

$$m_l c_0 = m_g + m_l c \tag{3.1}$$

Here c_0 is the initial concentration of gas dissolved in the liquid containing no bubbles and c is the gas concentration dissolved in the liquid in equilibrium with the bubble and is calculated using Henry's Law

$$c = Hp_g \tag{3.2}$$

with H being Henry's Law constant. The gas pressure in the bubble is given as

$$p_g = p_{atm} + \frac{2\sigma}{R_b} \tag{3.3}$$

The mass of the gas in the bubble is calculated using the ideal gas law

$$m_g = \frac{p_g \frac{4}{3}\pi R_b^3}{R_g T} \tag{3.4}$$

By substituting Equation (3.2), Equation (3.3), and Equation (1.4) into Equation (3.1) one can derive the equation for the gas balance in the cell in the following dimensionless form:

$$\frac{c_0}{c_s}-1=\Phi\left(\overline{R}_b\right)\equiv\frac{2\overline{\sigma}}{\overline{R}_b}+\frac{2\overline{\sigma}\overline{R}_b^2}{\overline{\rho}_l c_s}+\frac{\overline{R}_b^3}{\overline{\rho}_l c_s} \tag{3.5}$$

The function $\Phi\left(\overline{R}_b\right)$ is presented in Figure 28 with the horizontal dashed line representing $\frac{c_0}{c_s}-1$.

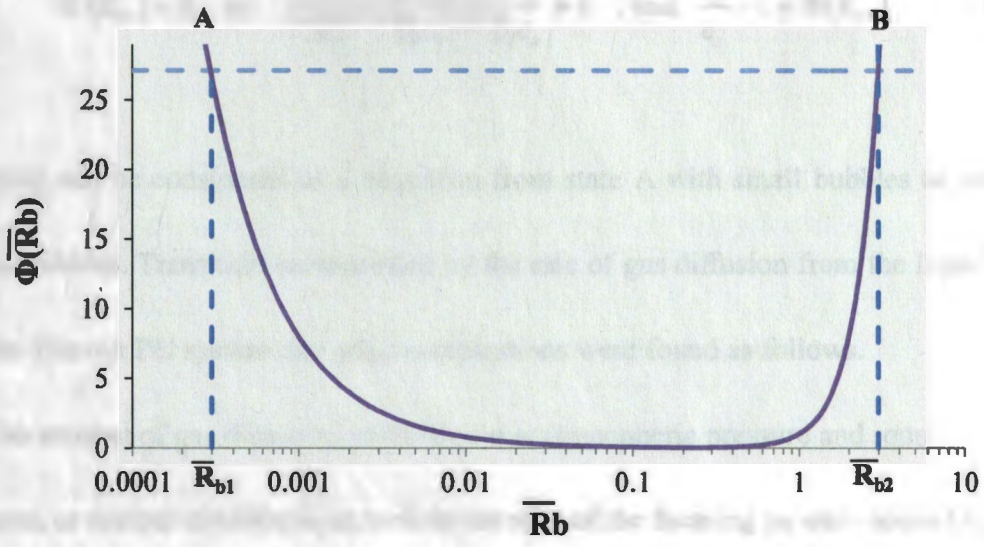

Figure 28. Solution to Equation (3.5).

One can see that if the initial concentration of gas dissolved in the liquid (c_0) is larger than some critical value (c_*) there are two steady bubble sizes $\overline{R}_{b1}$ (3×10^{-4}) and $\overline{R}_{b2}$ (2.98) which correspond to two different steady gas concentrations in the cell

$$\frac{c_1}{c_s} = 1 + \frac{2\overline{\sigma}}{\overline{R}_{b1}}, \quad \frac{c_2}{c_s} = 1 + \frac{2\overline{\sigma}}{\overline{R}_{b2}} \tag{3.6}$$

The critical gas concentration c_* was calculated as 1.82 x 10^{-3}, and was found using the following relations

$$\Phi'(\overline{R}_{b*}) = 0, \text{ or } -\frac{2\overline{\sigma}}{\overline{R}_b^2} + \frac{4\overline{\sigma}\overline{R}_b}{\overline{\rho}_l c_s} + \frac{3\overline{R}_b^2}{\overline{\rho}_l c_s} = 0 \text{ , and } \frac{c_*}{c_s} - 1 = \Phi(\overline{R}_{b*}) \tag{3.7}$$

Foaming can be considered as a transition from state A with small bubbles to state B with large bubbles. Transition is controlled by the rate of gas diffusion from the liquid into the bubble. For our PU system, the gas concentrations were found as follows.

The amount of gas dissolved in the liquid at atmospheric pressure and room temperature, or normal conditions, as well as the start of the foaming process needed to be determined for use in the modeling. In order to determine the concentration of gas dissolved at normal conditions, the ideal gas law equation

$$p_{atm} v_g = \frac{m_g}{M} RT \tag{3.8}$$

was used with v_g being the volume of gas and M the molar mass. Equation (3.8) was used along with the equation for the gas concentration

$$c_s = Hp_{atm} = \frac{m_g}{m_l} \tag{3.9}$$

with m_g, m_l being the mass of gas and liquid in the system. Solving for the mass in Equation (3.8) and substituting it into Equation (3.9), yields the equation

$$c_s = p_{atm}\left[\frac{v_g M}{RTm_l}\right] \tag{3.10}$$

By knowing the molar mass of CO_2 (44 kg/k mol), the gas constant, R (8.31 J/K mol) and the temperature, T (300 K), and the density of the liquid (1030 kg/m^3) the value of c_s in terms of the volume of gas to volume of liquid ratio was found to be

$$c_s = 0.00174\frac{v_g}{v_l} \tag{3.11}$$

with v_g and v_l being equal to the volume of gas and volume of liquid in the system.

For this system, the amount of water added is 2% by weight, or 20 g of H_2O per kg of liquid. With water having a molar mass of 18 g/mol, the amount of water added to the

system is 1.11 moles. Knowing that one mole of water generates one mole of carbon dioxide gas during the foaming process, the mass of CO_2 generated can be calculated by multiplying the molar mass of carbon dioxide by the moles of CO_2 generated by the system, 1.11 moles. The initial oversaturated concentration of gas to liquid in the system is found to be,

$$c_0 = \frac{48.9g(CO_2)}{1000g(liquid)} = 4.89 \times 10^{-2} \tag{3.12}$$

An assumption was made that the volume of gas to volume of liquid ratio was one to one, making c_s equal to $1.74\ x\ 10^{-3}$ kg/kg. When comparing this value to the initial oversaturated concentration, it can be seen that the system contains significantly more gas than would be achievable under normal conditions. Therefore, this system has a large driving force to encourage and allow for foaming.

The diffusion of dissolved gas in the cell is described by the equation

$$\frac{\partial c}{\partial t} + u_l \frac{\partial c}{\partial r} = \frac{D}{r^2} \frac{\partial}{\partial r}\left(r^2 \frac{\partial c}{\partial r} \right) \tag{3.13}$$

where $c(r,t)$ is gas concentration distribution in the liquid and D is the gas diffusion coefficient in liquid. The Equation (3.13) is complemented with the initial and boundary conditions:

$$\begin{aligned} c\big|_{t=0} &= c_1, \\ c\big|_{r=R_b} &= Hp_g, \\ \left.\frac{\partial c}{\partial r}\right|_{r=R_c} &= 0 \end{aligned} \tag{3.14}$$

The first equation of Equation (3.14) states that initially liquid is in the state A, filled with small bubbles of size R_{bl} and the gas concentration in the liquid is c_l. The second equation of Equation (3.14) states that current gas concentration at the bubble/liquid interface is proportional to current gas pressure, with H being Henry's constant. The third equation of Equation (3.14) states that there is no diffusion flux out of the cell.

It is more convenient to transform the Equations (3.13), (3.14) using Lagrangian coordinates

$$\xi = \frac{4}{3}\pi\rho_l(t)\left[r^3 - R_b^3(t)\right], \quad 0 < \xi < m_l, \quad R_b < r < R_c \tag{3.15}$$

Then the derivatives are transformed in the following way:

$$\left(\frac{\partial}{\partial t}\right)_r = \left(\frac{\partial}{\partial t}\right)_\xi + \left(\frac{\partial \xi}{\partial t}\right)_r \left(\frac{\partial}{\partial \xi}\right)_t = \left(\frac{\partial}{\partial t}\right)_\xi + \left(-4\pi\rho_l R_b^2 \dot{R}_b + \frac{d\ln\rho_l}{dt}\xi\right)\left(\frac{\partial}{\partial \xi}\right)_t$$
$$\left(\frac{\partial}{\partial r}\right)_t = \left(\frac{\partial \xi}{\partial r}\right)_t \left(\frac{\partial}{\partial \xi}\right)_t = 4\pi\rho_l r^2 \left(\frac{\partial}{\partial \xi}\right)_t, \qquad r = \left(\frac{3\xi}{4\pi\rho_l} + R_b^3\right)^{1/3} \tag{3.16}$$

Equation (3.13) and the conditions (3.14) will look as following:

$$\frac{\partial c}{\partial t} = 16\pi^2 \rho_l^2 D \frac{\partial}{\partial \xi}\left[\left(\frac{3\xi}{4\pi\rho_l} + R_b^3\right)^{4/3} \frac{\partial c}{\partial \xi}\right] \tag{3.17}$$

$$c\big|_{t=0} = c_1, \tag{3.18}$$

$$c\big|_{\xi=0} = Hp_g \tag{3.19}$$

$$\left.\frac{\partial c}{\partial \xi}\right|_{\xi=m_l} = 0 \tag{3.20}$$

First, an approximate solution was developed for the diffusion problem (Equations (3.17)-(3.20)), for the beginning of the foaming process when the diffusion boundary layer did not yet reach the liquid cell's boundary, based on simple parabolic approximation of concentration distribution

$$c(\xi,t) = c_1 + \left[Hp_g(t) - c_1\right]\left[1 - \frac{\xi}{\delta(t)}\right]^2 \tag{3.21}$$

Here $\delta(t)$ is the thickness of diffusion boundary layer around the bubble, which grows while diffusion proceeds up to the moment $t = t_b$ when it reaches $\delta(t)=m_l$. The solution (Equation(3.21)) is designed to satisfy boundary condition (Equation(3.19)) at the bubble interface. Also the condition (Equation(3.20)) is fulfilled naturally, because the following conditions are satisfied at the diffusion front and between diffusion from and liquid cell boundary:

$$\begin{aligned} &\xi = \delta(t): \quad c = c_1, \quad \frac{\partial c}{\partial \xi} = 0 \\ &\delta(t) < \xi < m_l: \quad c = c_1 \end{aligned} \tag{3.22}$$

The gas concentration distribution in the cell (Equation(3.21)) is presented schematically in Figure 29.

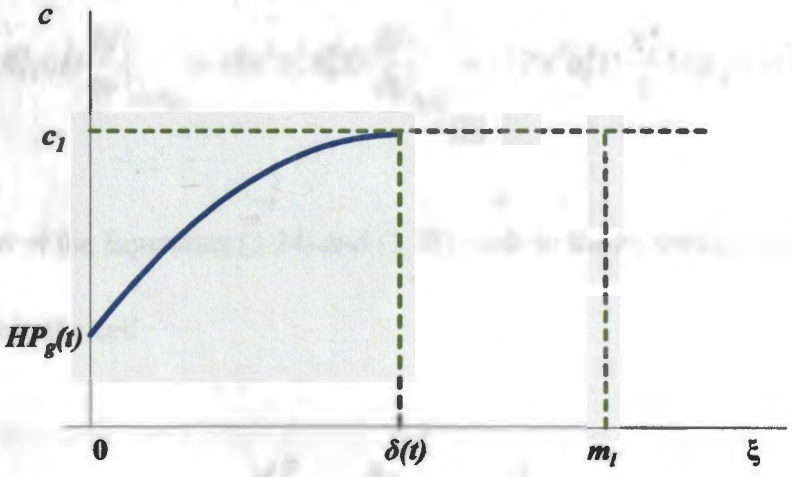

Figure 29. Changing gas concentration during State 1.

This distribution cannot satisfy the Equation (3.17), but is required that it satisfies the Equation (3.17) space integrated over the boundary layer

$$\frac{\partial}{\partial t}\int_0^{\delta(t)}\tilde{c}(\xi,t)d\xi = -16\pi^2\rho_l^2 D R_b^4 \left.\frac{\partial \tilde{c}}{\partial \xi}\right|_{\xi=0}, \quad \tilde{c} = c - c_1 \tag{3.23}$$

Further substitution the solution (3.21) in the Equation (3.23) leads to the following differential equation for unknown thickness of boundary layer $\delta(t)$

$$\frac{d}{dt}\left[\frac{\delta}{3}\left(Hp_g - c_1\right)\right] = 32\pi^2\rho_l^2 D\frac{R_b^4}{\delta}\left(Hp_g - c_1\right) \tag{3.24}$$

Gas mass in the bubble m_g is calculated from the following mass balance

$$\frac{dm_g}{dt} = 4\pi R_b^2\rho_l D\left.\frac{\partial \tilde{c}}{\partial r}\right|_{r=R_b} = 16\pi^2\rho_l^2 R_b^4 D\left.\frac{\partial \tilde{c}}{\partial \xi}\right|_{\xi=0} = -32\pi^2\rho_l^2 D\frac{R_b^4}{\delta}\left(Hp_g - c_1\right) \tag{3.25}$$

Summation of the Equations (3.24) and (3.25) leads to the following form of gas mass conservation in the cell

$$\frac{d}{dt}\left[m_g + \frac{\delta}{3}\left(Hp_g - c_1\right)\right] = 0 \tag{3.26}$$

After integration over time and using the Equations (3.3) and (3.4) the following integral of mass is found

$$\frac{\left(p_{atm}+\frac{2\sigma}{R_b}\right)\frac{4}{3}\pi R_b^3}{R_g T}+\frac{\delta}{3}\left(c_s+\frac{2\sigma H}{R_b}-c_l\right)=M=const \tag{3.27}$$

The mass of gas in the cell is calculated at state A (see Figure 28)

$$M=\frac{\left(p_{atm}+\frac{2\sigma}{R_{b1}}\right)\frac{4}{3}\pi R_{b1}^3}{R_g T} \tag{3.28}$$

Combination of Equations (3.27) and (3.28) leads to the algebraic equation showing how diffusion boundary layer thickness change with bubble radius

$$\delta(R_b)=\frac{4\pi}{R_g T}\frac{\left(p_{atm}+\frac{2\sigma}{R_b}\right)\frac{4}{3}\pi R_b^3-\left(p_{atm}+\frac{2\sigma}{R_{b1}}\right)\frac{4}{3}\pi R_{b1}^3}{c_l-c_s-\frac{2\sigma H}{R_b}} \tag{3.29}$$

which in dimensionless variables looks as following

$$\bar{\delta} = \frac{3}{\bar{\rho}_l c_s} \frac{\bar{R}_b^3 + 2\bar{\sigma}\bar{R}_b^2 - \left(\bar{R}_{b1}^3 + 2\bar{\sigma}\bar{R}_{b1}^2\right)}{\bar{c}_1 - 1 - \dfrac{2\bar{\sigma}}{\bar{R}_b}}, \quad \bar{\delta} = \frac{\delta}{m_l}, \quad \bar{c}_1 = \frac{c_1}{c_s} \tag{3.30}$$

The Equation (3.25) using the Equations (3.3) and (3.4) can be transformed into the following differential equation for growing bubble radius

$$\frac{dR_b}{dt} = -8\pi\rho_l^2 D R_g T \frac{R_b^3}{\delta(R_b)} \frac{Hp_{atm} + \dfrac{2\sigma H}{R_b} - c_1}{p_{atm} R_b + \dfrac{4}{3}\sigma} \tag{3.31}$$

which in the dimensionless form looks as following

$$\frac{d\bar{R}_b}{d\bar{t}} = 6\bar{\rho}_l c_s \frac{\bar{R}_b^3}{\bar{\delta}(\bar{R}_b)} \frac{\bar{c}_1 - 1 - \dfrac{2\bar{\sigma}}{\bar{R}_b}}{\bar{R}_b + \dfrac{4}{3}\bar{\sigma}}, \quad \bar{t} = \frac{t}{\tau_D}, \quad \tau_D = \frac{R_0^2}{D} \tag{3.32}$$

The Equation (3.32) together with Equation (3.30) should be solved using initial condition

$$\bar{R}_b(0) = \bar{R}_{b1} \tag{3.33}$$

until the moment $\bar{t} = \bar{t}_b$ when $\bar{\delta}(\bar{R}_b) = 1$, when diffusion boundary layer will reach the liquid cell boundary. After that moment another parabolic approximation of

concentration distribution was used:

$$c(\xi,t) = Hp_g(t) + B(t)\left(2m_l\xi - \xi^2\right) \tag{3.34}$$

Here $B(t)$ is the unknown coefficient which changes while diffusion proceeds. The solution (Equation (3.34)) is designed to satisfy boundary condition (Equation(3.19)) at the bubble interface, and (Equation (3.20)) at liquid cell boundary. Gas concentration distribution in the cell (Equation (3.21)) is presented schematically in Figure 30.

This distribution cannot satisfy the Equation (3.17), but we will require that it satisfies the Equation (3.17) space integrated over the liquid cell

$$\frac{\partial}{\partial t}\int_0^{m_l} c(\xi,t)d\xi = -16\pi^2\rho_l^2 DR_b^4 \left.\frac{\partial c}{\partial \xi}\right|_{\xi=0} \tag{3.35}$$

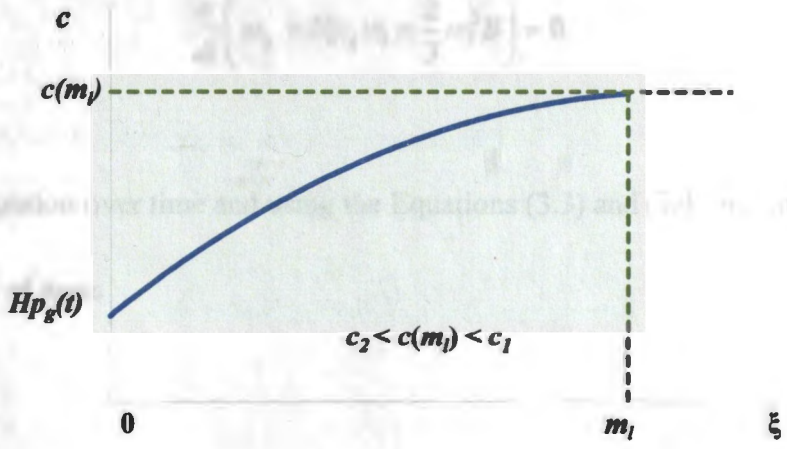

Figure 30. Changing gas concentration during State 2.

Further substitution the solution (3.34) in the Equation (3.35) leads to the following differential equation for unknown parameter $B(t)$

$$\frac{d}{dt}\left(Hp_g + \frac{2}{3} m_l^2 B \right) = -32\pi^2 \rho_l^2 D R_b^4 B \tag{3.36}$$

Gas mass in the bubble m_g is calculated from the following mass balance

$$\frac{dm_g}{dt} = 4\pi R_b^2 \rho_l D \left.\frac{\partial c}{\partial r}\right|_{r=R_b} = 16\pi^2 \rho_l^2 R_b^4 D \left.\frac{\partial c}{\partial \xi}\right|_{\xi=0} = 32\pi^2 \rho_l^2 D m_l R_b^4 B \tag{3.37}$$

Summation of the Equation (3.36) multiplied by m_l and the Equation (3.37) leads to the following form of gas mass conservation in the cell

$$\frac{d}{dt}\left(m_g + Hp_g m_l + \frac{2}{3} m_l^3 B \right) = 0 \tag{3.38}$$

After integration over time and using the Equations (3.3) and (3.4) one can get the following integral of mass

$$\frac{\left(p_{atm}+\frac{2\sigma}{R_b}\right)\frac{4}{3}\pi R_b^3}{m_l R_g T}+c_s+\frac{2\sigma H}{R_b}+\frac{2}{3}m_l^2 B = M = const \tag{3.39}$$

Mass of the gas in the cell is calculated at state B (see Figure 28)

$$M=\frac{\left(p_{atm}+\frac{2\sigma}{R_{b2}}\right)\frac{4}{3}\pi R_{b2}^3}{m_l R_g T}+c_s+\frac{2\sigma H}{R_{b2}} \tag{3.40}$$

Combination of Equation (3.39) and Equation (3.40) leads to the algebraic equation showing how parameter B changes with bubble radius

$$\frac{2}{3}m_l^2 B=\frac{2\sigma H}{R_{b2}}+\frac{\left(p_{atm}+\frac{2\sigma}{R_{b2}}\right)\frac{4}{3}\pi R_{b2}^3}{m_l R_g T}-\left[\frac{2\sigma H}{R_b}+\frac{\left(p_{atm}+\frac{2\sigma}{R_b}\right)\frac{4}{3}\pi R_b^3}{m_l R_g T}\right] \tag{3.41}$$

which in dimensionless variables looks as follows

$$\overline{B}=\Phi\left(\overline{R}_{b2}\right)-\Phi\left(\overline{R}_b\right),\quad \overline{B}=\frac{2m_l^2}{3Hp_{atm}}B \tag{3.42}$$

where function $\Phi(\overline{R}_b)$ is defined by the Equation (3.5). The Equation (3.37) using the Equation (3.4) can be transformed into the following differential equation for growing bubble radius

$$\frac{dR_b}{dt} = 8\pi\rho_l^2 Dm_l R_g T \frac{R_b^3 B}{p_{atm} R_b + \frac{4}{3}\sigma} \tag{3.43}$$

which in the dimensionless form looks as follows

$$\frac{d\overline{R}_b}{d\overline{t}} = 9\overline{\rho}_l c_s \frac{\overline{R}_b^3 \overline{B}(\overline{R}_b)}{\overline{R}_b + \frac{4}{3}\overline{\sigma}}, \quad \overline{t} = \frac{t}{\tau_D}, \quad \tau_D = \frac{R_0^2}{D} \tag{3.44}$$

The Equation (3.44) together with Equation (3.32) should be solved using the initial condition

$$\overline{R}_b(t_b) = \overline{R}_b\Big|_{\overline{\delta}(t_b)=1} \tag{3.40}$$

A radius versus time curve is presented in Figure 31.

Similar to the viscosity controlled model, the entire bubble growth occurs in less than a second, which is much faster than is seen in experimental work. This shows that the diffusion of gas through the liquid during the foaming reaction is not the limiting factor to the growth of the foam. Therefore, the polymerization kinetics are found to play a role

in the time to expand or fill the mold. In applications where the polyurethane is formulated to react at times of less than a second, these models may more closely predict the foam growth rate.

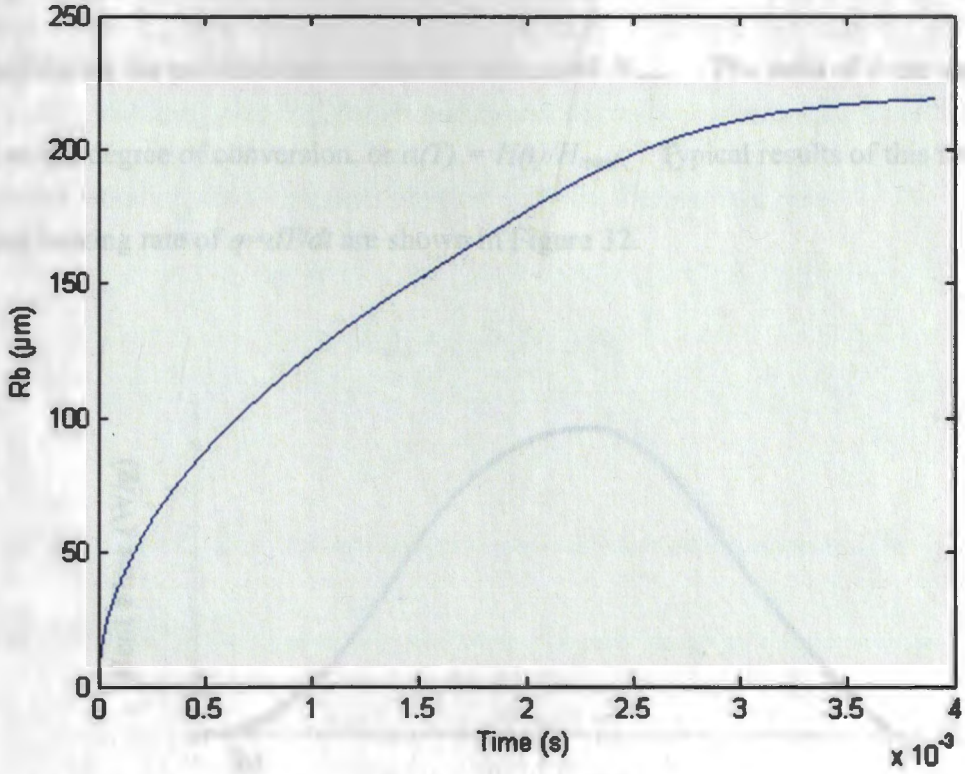

Figure 31. Change in bubble radius as a function of time.

5.3. Polymerization Kinetics

5.3.1. Polymerization Kinetics Procedure

The polymerization kinetics of the curing polyurethane liquids were examined for the system of liquids used in this research. The reaction kinetics were analyzed by using

DSC, which measures the heat evolution caused by the reaction of polymerization, as was shown in research [61]. A polymerization development in time is normally characterized by heat generated during cure time (from the initial moment, $t = 0$, to some current moment, t). This generated heat is denoted as $H(t)$ and is measured in J/m^3. The total heat generated during the polymerization process is denoted H_{total}. The ratio of these values is defined as the degree of conversion, or $\alpha(T) = H(t)/H_{total}$. Typical results of this method at a constant heating rate of $q=dT/dt$ are shown in Figure 32.

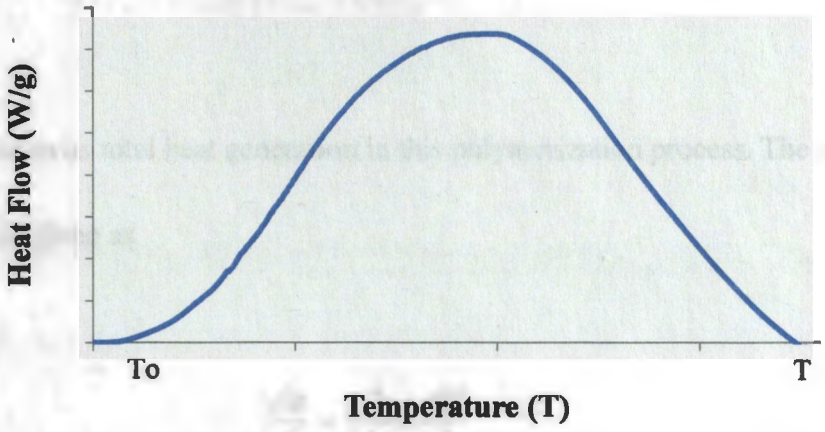

Figure 32. Differential scanning calorimetry results for a constant q.

The total heat generated during full conversion, rate of conversion, and the activation energy of the system were found using the following equations. The total heat generated during the process of full conversion time was given as

$$H_{total} = \int_{T_o}^{\infty} \frac{dH}{dt}(T)\frac{dT}{q} \tag{4.1}$$

with *dH/dt* being the heat flow, and q the constant heating rate at which the run was performed. The experiments were conducted for several different heat rates ($q_i = 1,2,...N$). Each experimental line gives $H_{total}(q_i)$. Some experimental scatter may take place due to experimental errors or some unknown physical reasons. The average value

$$H_{total} = \frac{1}{N}\sum_{i=1}^{N} H_{total}(q_i) \tag{4.2}$$

will be taken as total heat generation in this polymerization process. The degree of conversion rate is given as

$$\frac{d\alpha}{dt} = \frac{1}{H_{total}}\frac{dH}{dt} \tag{4.3}$$

with α being the conversion of the liquid polymer and *dα/dt* being the conversion rate. The conversion rate can be calculated using Figure 32 and is presented schematically in Figure 33.

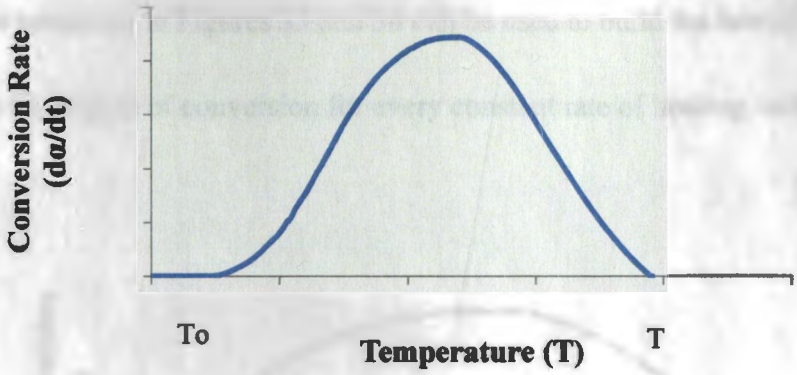

Figure 33. Schematic of conversion rate versus temperature.

The degree of conversion of the polymer as a function of temperature was found with

$$\alpha(T) = \int_{T_o}^{T} \frac{d\alpha}{dt}(T)\frac{dT}{q} \tag{4.4}$$

for each of the heating rates used. The solution of this equation is presented schematically in Figure 34.

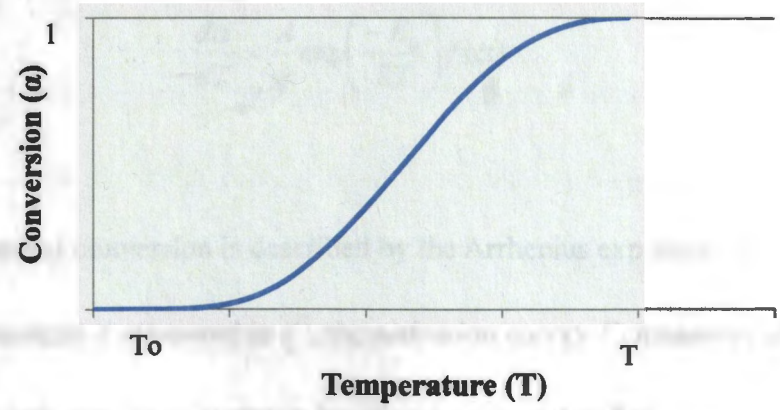

Figure 34. Schematic of conversion versus temperature.

The curves presented in Figures 33 and 34 can be used to build the rate of conversion versus the degree of conversion for every constant rate of heating, as shown in Figure 35.

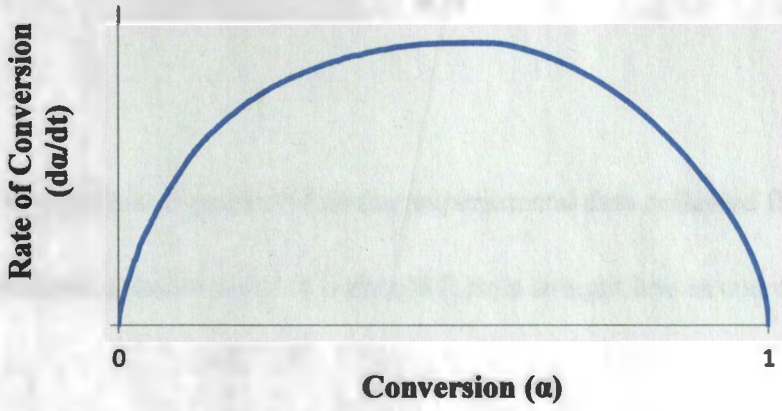

Figure 35. Schematic of rate of conversion versus conversion.

The data presented in the previous curves can be used to identify the parameters of the polymerization kinetics model. The simplest version of which is presented in the following equation

$$\frac{d\alpha}{dT} = \frac{A}{q}\exp\left(\frac{-E_a}{RT}\right)f(\alpha) \tag{4.5}$$

Here the rate of conversion is described by the Arrhenius expression with the pre-exponential constant A measured in s^{-1}, the activation energy E_a measured in J/mol, the universal gas constant, and the conversion functional relationship $f(\alpha)$.

To come up with algorithm of calculation of the activation energy from the experimental data it is useful to transform the Equation (4.5) into the following relation

$$\ln\left(\frac{d\alpha}{dt}\right) = \ln[A f(\alpha)] - \frac{E_a}{R}\frac{1}{T} \tag{4.6}$$

It is clearly visible from Equation (4.6) that experimental data collected from the Figures 33-35 for selected constant value of α should form a straight line in coordinates

$$X = \frac{1}{T}, \quad Y = \ln\left(\frac{d\alpha}{dt}\right) \tag{4.7}$$

as follows

$$Y = a - bX, \quad a = \ln[A f(\alpha)], \quad b = \frac{E_a}{R} \tag{4.8}$$

One can plot the experimental data for some constant α as shown schematically in Figure 36 and calculate E_a for this particular α. The activation energy (E_a) is taken as the tangent of the angle the best fit line makes with the y-axis multiplied by the universal gas constant, assuming it does not vary much with the degree of conversion. A schematic of this can be seen below in Figure 36.

Repeating this procedure for different α, one may come up with dependency $E_a(\alpha)$. If it is determined that the dependency $E_a(\alpha)$ is not very strong, the average value of E_a may be taken for all used values of α and used as the constant activation energy for this polymerization process.

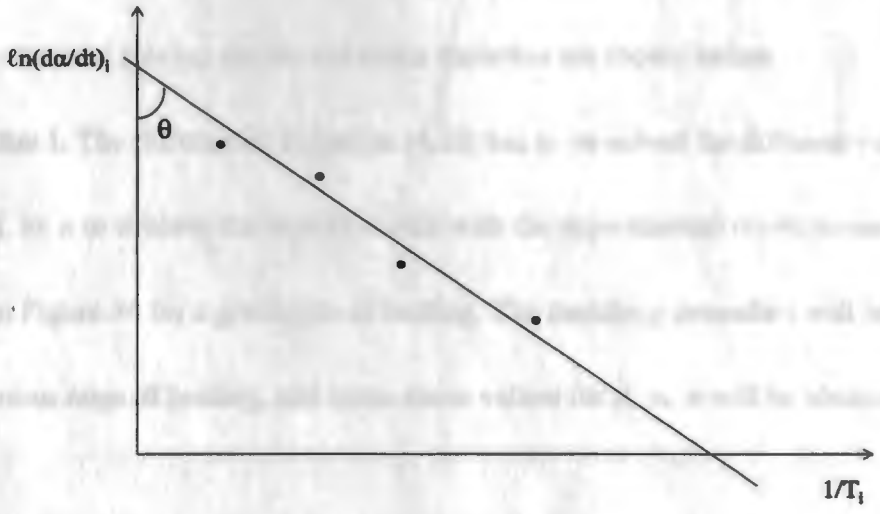

Figure 36. Schematic of determination of activation energy for a constant α.

To determine the pre-exponential constant A, and the conversion functional relationship $f(\alpha)$ from experimental data an explicit form for $f(\alpha)$ should be assumed. One of the simplest so-called autocatalytic models that can mimic the shape presented schematically in Figure 34 looks as follows

$$f(\alpha) = \alpha^m (1-\alpha)^n \tag{4.9}$$

where m and n are reaction orders. In case of constant heating rate ($q = const$) the kinetic Equations (4.5), (4.9) can be represented in the following form

$$\frac{d\alpha}{dT} = \frac{A}{q}\exp\left(-\frac{E_a}{RT}\right)\alpha^m(1-\alpha)^n \tag{4.10}$$

The two ways of solving for the unknown variables are shown below.

Algorithm I. The differential Equation (4.10) has to be solved for different values of parameters A, m, n to achieve the best-fit match with the experimental curve presented schematically in Figure 34 for a given rate of heating. The matching procedure will be repeated for various rates of heating, and some mean values for A, m, n will be obtained.

Algorithm II. Theoretically the Equation (4.10) can be integrated using the method of separation of variables as following

$$\int_0^{\alpha}\frac{d\alpha}{\alpha^m(1-\alpha)^n} = \frac{AE_a}{qR}\int_{\beta}^{\infty}\frac{\exp(-\beta)}{\beta^2}d\beta\,, \quad \beta = \frac{E_a}{RT} \tag{4.11}$$

It is clearly visible from Equation (4.11) that experimental data collected from the Figures 33-35 for selected constant heating rate q should form a straight line in coordinates

$$X = \frac{E_a}{qR}\int_{\beta}^{\infty}\frac{\exp(-\beta)}{\beta^2}d\beta\,, \quad Y = \int_{0}^{\alpha}\frac{d\alpha}{\alpha^m(1-\alpha)^n}\,, \quad \beta = \frac{E_a}{RT} \tag{4.12}$$

as follows

$$Y = AX \tag{4.13}$$

Where A is the pre-exponential constant that should be determined. The experimental data may be plotted for a selected constant heating rate q, and for some fixed unknown yet reaction orders m and n, as shown schematically in Figure 37, and calculate A for this particular q.

Repeating this procedure for different q, one may put all these experimental points (X,Y) in one plot and come up with some mean value of A for some fixed unknown reaction of orders m and n. Then, the procedure should be repeated for various reaction orders m and n to achieve a better linear fit.

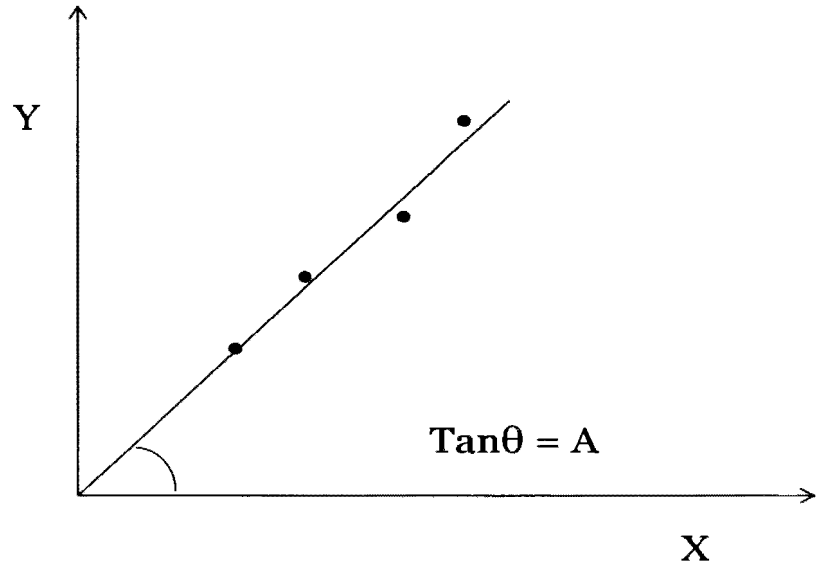

Figure 37. Schematic for the determination of unknown value A.

5.3.2. Polymerization Kinetics Results

The results of the polymerization kinetics for the polyurethane foam used in this research are shown below. Due to the complexity of the foaming and curing reactions, these results were not incorporated into the model for the foam growth, but are shown for possible use in future investigation into the foaming process. Both TGA and DSC results are shown along with the kinetics modeling results.

5.3.2.1. Thermogravimetric Analysis Results

Thermogravimetric analysis (TGA) was performed to examine the percentage moisture and decomposition properties for both the polyol and isocyanate liquids at atmospheric conditions. The isocyanate was shown to decompose between 250 °C and 300 °C, while

the polyol showed decreases in the weight loss at two different temperature ranges. The first significant decrease in weight begins at 200 °C and the second at 350 °C. The isocyanate, having only one drop in weight percentage, has a less complex structure when compared to the polyol. This can also be seen when examining the chemical structure of each of these liquids (Figure 4). An example of the TGA results can be seen below.

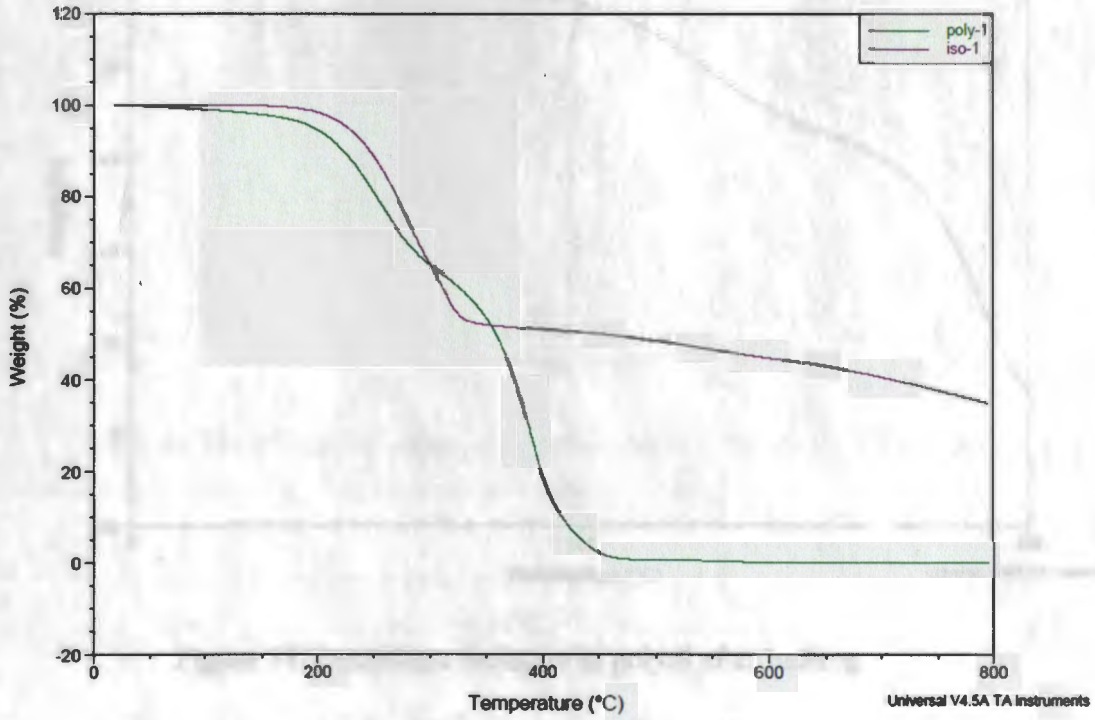

Figure 38. TGA results for polyol and isocyanate liquids.

5.3.2.2. Differential Scanning Calorimetry Results

In order to keep the foaming polyurethane from escaping from the pan during the test, the foaming agent (water) was removed from the polyol. The polyol was put into a

glass container and heated on a hot plate for sixty minutes at 120 °C to remove the water. The TGA results show a sample of the polyol heated to 120 °C and held for sixty minutes in the insulated furnace. It can be seen in Figure 39 that the added 2% water by weight would be fully removed after this process was completed.

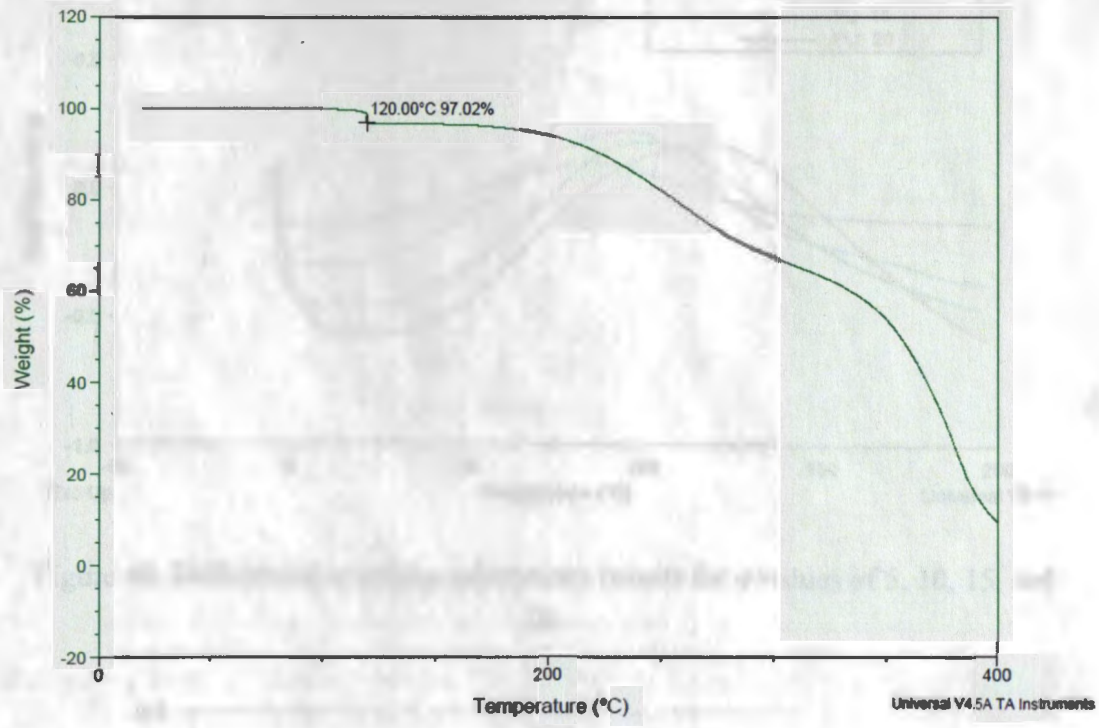

Figure 39. Percentage moisture in polyol after heating.

Figure 40 shows the results of DSC experiments for the curing reaction of the non-foaming polyurethane at rates of 5 °C/min, 10 °C/min, 15 °C/min, and 20 °C/min.

The total heat was found from the area under the curve of each of the heat flow plots. By adjusting the curves to an equal starting point, it can be seen in Figure 41 that with an increase in heating rate, the area under the curve increases. Normalizing these

values with the heating rate used for each experiment (Equation (4.1)) resulted in a nearly constant value for the total heat, with the average being 206 J/g ± 9.3.

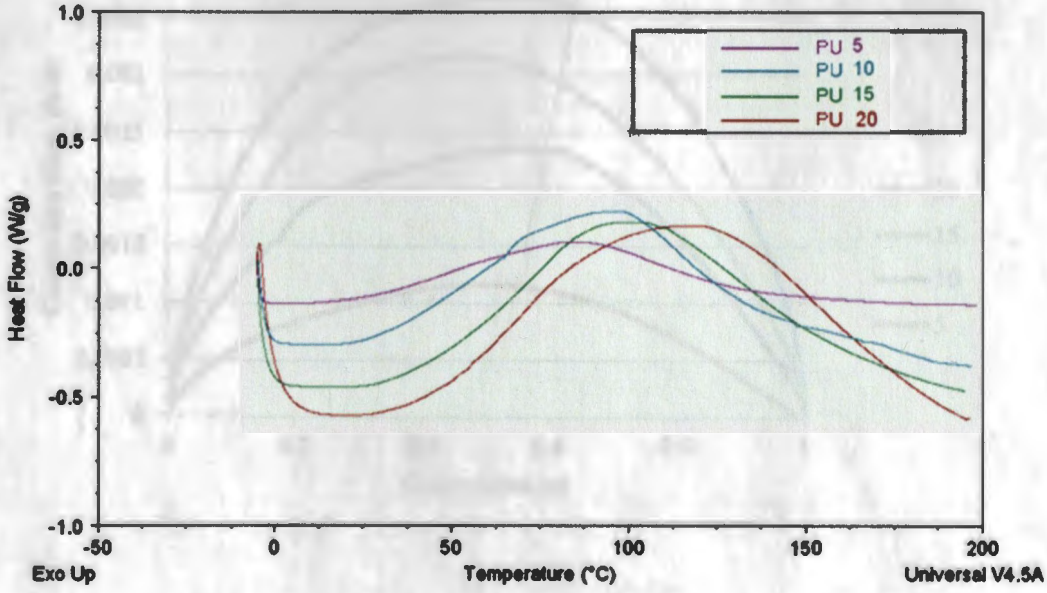

Figure 40. Differential scanning calorimetry results for q values of 5, 10, 15, and 20.

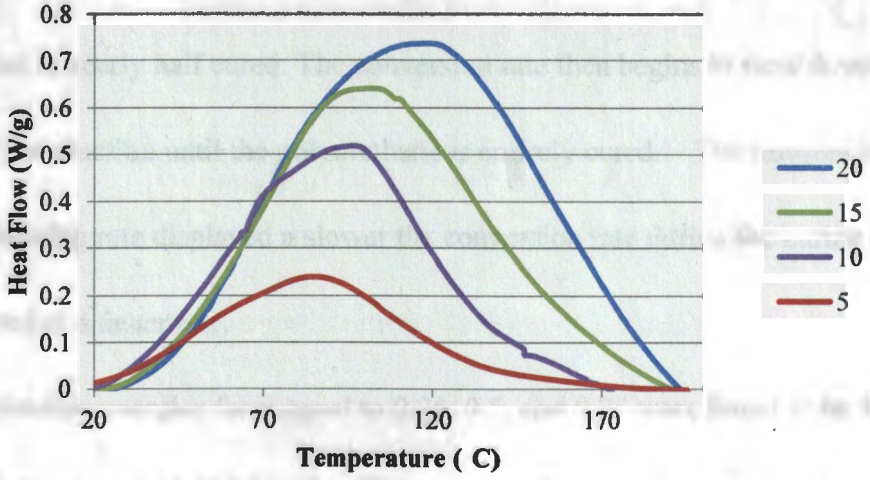

Figure 41. Heat flow versus temperature.

The conversion of the liquid polymer and conversion rate were also determined for each of the heating rates examined and the results are shown in Figure 42.

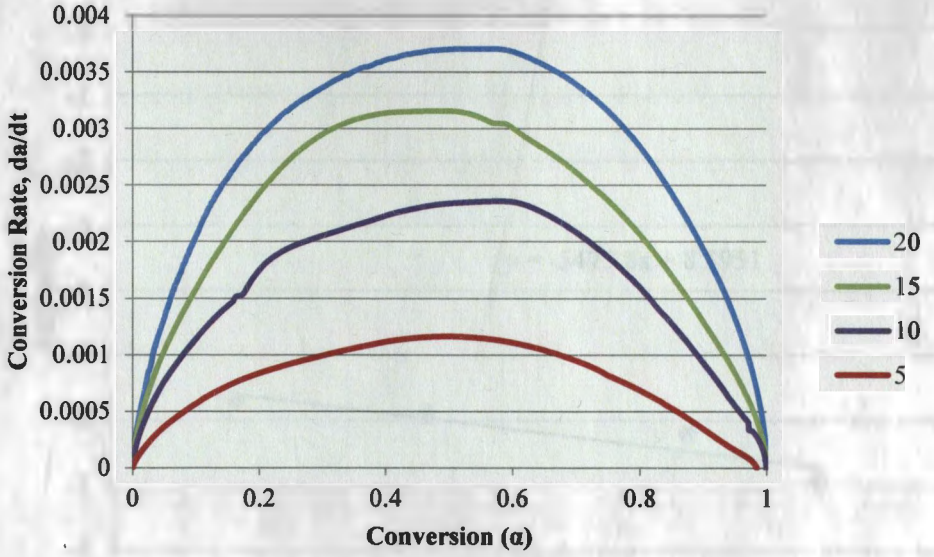

Figure 42. Conversion rate as a function of conversion.

It is seen that as the reaction begins slowly, with the conversion rate increasing until the polyurethane is nearly half cured. The conversion rate then begins to slow down during the last half of the reaction until the polyurethane is entirely cured. The samples heated with a slower heating rate displayed a slower the conversion rate during the curing event than those heated at a faster rate.

The activation energies for α equal to 0.25, 0.5, and 0.75 were found to be 48.63 kJ/mol, 42.42 kJ/mol, and 45.33 kJ/mol. The average of these values was used as the

activation energy for the polyurethane and was found to be 45.46 kJ/mol ± 3.11. A plot of the determination of the activation energy can be seen below.

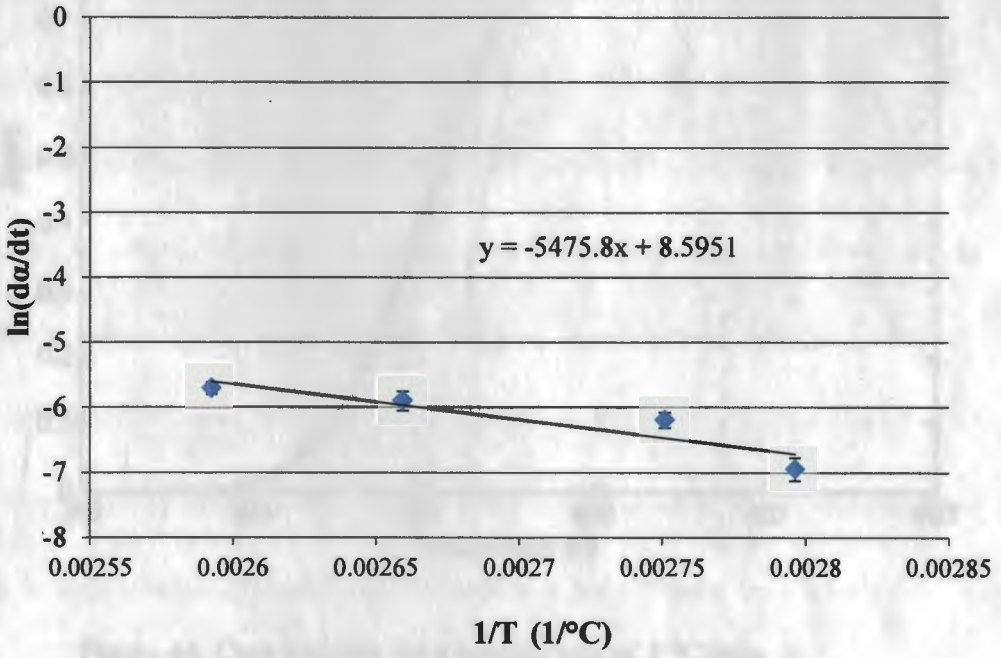

Figure 43. Determination of the activation energy for the average of three α values.

The cure kinetics were solved for the unknown variables *A*, *m*, and *n* using the Equation (4.10). The Algorithm I was used to solve for the variables and an example of the best fit curve for one of the heating rates can be seen in Figure 44 with the blue line being experimental results and the green line the solution of Equation (4.10).

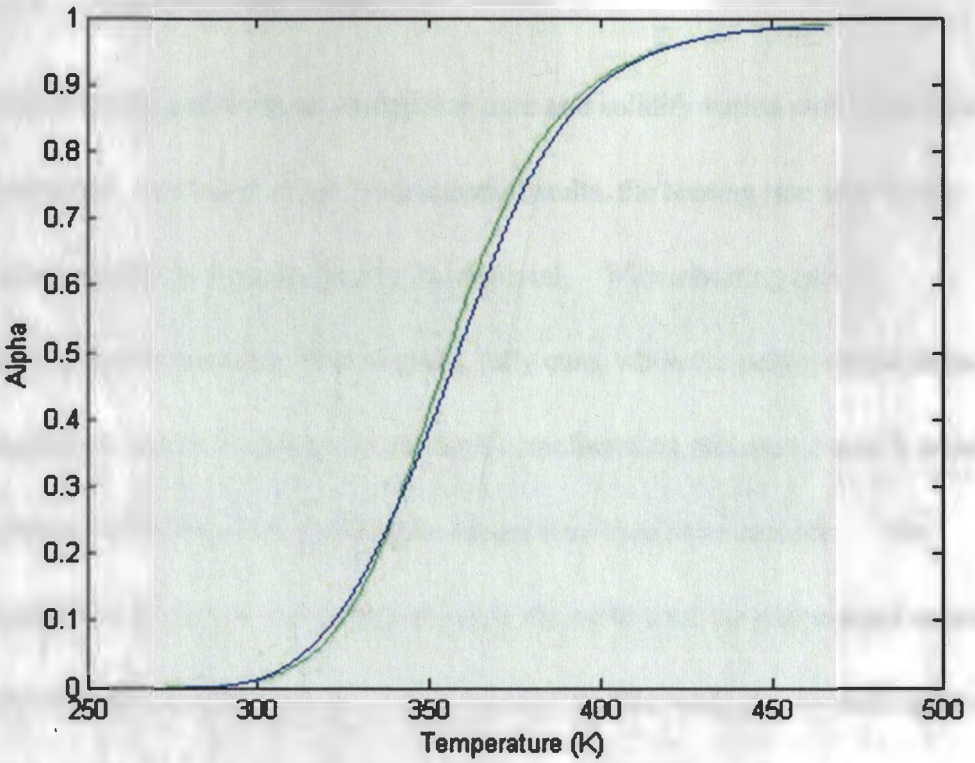

Figure 44. Cure kinetics for a heating rate of 5 °C/min.

A best fit line was found for each of the four heating rates by solving for the unknown *A*, *m*, and *n* values and comparing to experimental data. The results can be seen in the following table.

Table 4. Kinetics model variable results.

Heating Rate	°C/min	5	10	15	20	Average	St. Dev.
A	1/s	29000	40000	26500	18800	28575	8767
m		0.285	0.305	0.215	0.035	0.21	0.123
n		1.98	1.81	1.55	1.57	1.73	0.203

5.3.2.3. Demolding Time Prediction

The time for the polyurethane material to cure and solidify varied with temperature and mold geometry. As found in the experimental results, the heating rate used in the DSC work played a role in the cure time of the material. With a heating rate of 5°C/minute the polyurethane took 36 minutes to fully cure, while the polyurethane heated at 20°C/minute took only 9.5 minutes. In the SAS manufacturing process no heat is added to the part during the curing cycle, making the longer cure time more realistic. The process employed by SAS is to leave the part inside the mold until the temperature reduces to an acceptable handling temperature. Using Frame C in this work, the demolding time was found to be approximately 45 minutes, while Frame A and Frame B took only 30 minutes due to a lesser volume of material which cooled more quickly.

5.4. Heat Transfer Process Through the Foam Accompanied With Polymerization Heat Release

The foaming process in the liquid, in general, represents a simultaneous action of multiple phenomena, namely, diffusion between liquid and bubble in the foam cell, viscous damping of bubble growth in the foam cell, and heat release due to liquid polymerization in the cell. Due to heat exchange with the surroundings at the top and bottom plates and heat transfer through the foam (i.e. heat exchange between cells), the temperature distribution in

the foam may not always be uniform. The schematic of the foam temperature distribution across the sample is presented in Figure 45.

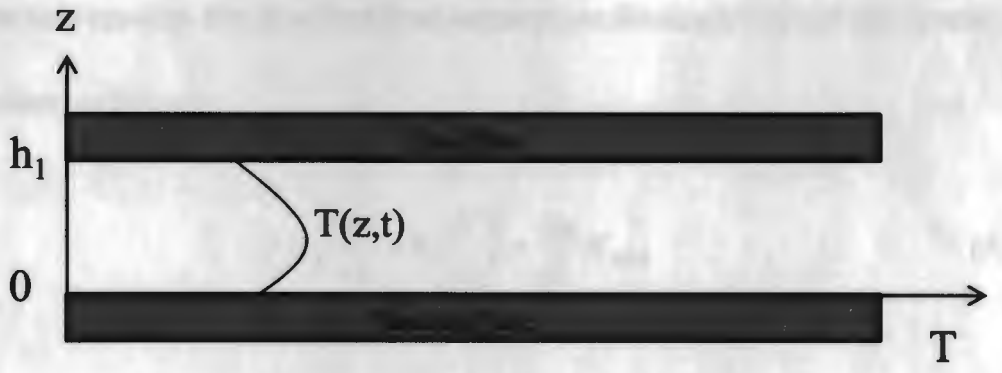

Figure 45. Temperature profile distribution throughout the foam sample.

Heat transfer within the foam may lead to redistribution of liquid pressure and temperature between the cells. Basically, the gas bubbles would grow differently in different foam cells, which would finally lead to non-uniform bubble size distribution across the foam sample.

However, at least for polymeric materials considered in this study, the characteristic time of diffusion and viscosity controlled bubble growth is much shorter than the characteristic time of liquid polymerization. That is why these two processes, bubble growth and liquid polymerization, can be separated in time. The assumption can be made that the bubble growth happens almost immediately while the temperature is uniform across the foam sample and is equal to room temperature. Then the bubble size along with

the gas and liquid pressure across foam sample can be calculated using the equilibrium scheme presented earlier. At this moment the polymerization begins.

The heat equation that describes foam temperature distribution across the sample was formulated as follows

$$\rho_f c_f \frac{\partial T}{\partial t} = k_f \frac{\partial^2 T}{\partial z^2} + \frac{\partial \alpha}{\partial t} H_{total} \tag{5.1}$$

which is combined with the equation of polymerization kinetics

$$\frac{\partial \alpha}{\partial t} = A \exp\left(-\frac{E_a}{RT}\right) \alpha^m (1-\alpha)^n \tag{5.2}$$

Here ρ_f, c_f, k_f are density, specific heat, and thermal conductivity of the foam, basically of the liquid bubble mixture, that in general depends on bubble volumetric concentration and bubble size.

As a simple approximation it can be accepted that

$$\rho_f = \rho_l (1-\varphi),\ c_f = c_l (1-\varphi),\ k_f = k_l (1-\varphi) \tag{5.3}$$

where φ is the volumetric concentration of bubbles in the foam; ρ_l, c_l, k_l are density, specific heat, and thermal conductivity of the liquid. It is accounted for that the density, specific heat, and thermal conductivity of the liquid is much larger than that of the gas. The volumetric concentration of bubbles in the foam was calculated knowing bubble size, and foam cell size as following

$$\varphi = \left(\frac{R_b}{R_c} \right)^3 \tag{5.4}$$

where the bubble size, and foam cell size were calculated in the equilibrium scheme.

The boundary conditions at the top plate and bottom plate are

$$\begin{aligned} k_f \left. \frac{\partial T}{\partial z} \right|_{z=0} &= \frac{k_B}{h_B} \left(T|_{z=0} - T_0 \right) \\ k_f \left. \frac{\partial T}{\partial z} \right|_{z=h_1} &= -\frac{k_T}{h_T} \left(T|_{z=h_1} - T_0 \right) \end{aligned} \tag{5.5}$$

where k_B, h_B, k_T, h_T are thermal conductivity and thickness of the bottom plate and top plate respectively.

Equations (5.1), (5.2), along with boundary conditions (5.5) would have to be solved using computational methods for partial differential equations. The solution of this problem would allow prediction of foam temperature and degree of conversion in any point of space and moment of time.

CHAPTER 6. CONCLUSIONS AND FUTURE WORK

6.1. Conclusions

The time to fill the mold was found during the pressure determination tests as the time until a load was seen by the load frame. The initial steady load was taken as the starting value for each of the tests. After an average of 70 seconds after placing the liquid in the mold an increase in the load was seen indicating the mold had been filled with the expanding foam. In reality, this value may be slightly longer due to the fact that the starting time of the experiment was taken after the liquids were mixed, or 20 seconds into the reaction. The amount of time for the material to cure and cool was found to be dependent on the volume of material as well as the mold material. A larger amount of PU foam will take a longer time to cool than a smaller volume. Also, an amount of PU foam in an insulating mold will retain heat much longer than a mold made of metal or another thermally conductive material. When molding new geometries for the first time, the liquid volume as well as the mold material should be taken into consideration when determining the amount of time the curing polyurethane will need to be left inside the mold.

The pressure created by the foam during the reaction was determined to increase with an increasing applied preload. This was due to the larger applied load minimizing the amount of material able to escape from the mold. The large preload may also have trapped

some gas that was initially inside the mold from escaping, which would increase the final pressure observed during the foaming process. An average pressure of 0.78 MPa was found to be generated by the foaming process of the rigid polyurethane foam.

In order to determine if the size of the frame played a role in the calculated maximum pressure, testing was done on two frames, one having twice the contact area of the other. The difference in size was found to play a role in the measured pressure created by the foam when including the frame area in the calculations. However, when using only the foam area to calculate the pressure generated, the size of the frame did not show any effect. The same pressure was calculated with Frame A and Frame B when having the same initial parameters (density and preload). A scaled up test was also conducted using Frame A and Frame C for comparison. The pressure measured using these frames was found to differ by 8.6%. This shows that the pressure generated may only be affected by the volume of material inside the frame.

To determine the rate of change of bubble size and final average diameter, several computer codes were created with the ability to alter the initial parameters (temperature, mold geometry, viscosity, surface tension, etc.) if necessary. The final average size of the bubble was found to be closely predicted using the equilibrium condition of the theoretical model created. Knowing the final bubble size may help to predict the final mechanical properties of the foam. However, the rate of change in cell size was predicted to occur

much faster than is seen experimentally. The theoretical modeling of the rate of change of bubble size examined the viscosity and diffusion effects of the liquids, but did not incorporate the curing kinetics of the polyurethane liquid due to complexity of the model. Incorporation of this information may lead to a more realistic prediction of the rate of bubble growth.

Several assumptions were made in order to create a more simplistic model of the foaming reaction. Each of these assumptions may lead to a certain amount of error in the results of the model. The assumption that upon initial mixing of the two liquids all of the CO_2 gas was generated and dissolved in the liquids may be a source of error in the model. In reality, the CO_2 will be generated as a function of time, not instantaneously, and may lead to a longer time period for the foaming reaction to occur. The determination of the concentrations of gas at saturation and the start of the reaction (c_s, c_0) were based on the chemistry of the reaction, but also an estimation of gas solubility in the liquids. The ratio of these values gives the drive towards foaming and a change in the ratio will affect the final results of the model. Also, the assumption that the glass loading does not play a large role in the foaming reaction may be incorrect and lead to a larger error in the results. The glass loading may impede or restrict the growth of the bubbles leading to a slower time than was seen experimentally. The glass may also contain a sizing material that could interact with the curing or foaming reactions.

6.2. Recommendations for Future Work

Future work based on this thesis would include an examination of the bubble growth in the x and y directions in addition to the z (height) direction presented in this research. This work would expand on the modeling already completed and use the same values and variables. The current model should be a close assumption of the foaming in the x and y direction with a change in orientation from the current examination. This is feasible since the bubble growth is not directional, but rather dependent on the constraints placed upon it by the mold it is contained inside.

In order to obtain a more realistic time scale for the bubble growth during the foaming reaction, the curing kinetics and temperature change would need to be incorporated into the model. Due to the curing liquids, an increase in viscosity and temperature will occur as a function of time and may lead to a slower growth of the foam. As was shown, the temperature within the foam increased from 20 °C to 140 °C during the cure reaction due to the exothermic reaction, which may lead to a non-uniform distribution of bubbles throughout the thickness of the foam sample. The experimental modeling presented in this body of work neglected the effects of this temperature change and curing kinetics due to simplifications of the model as a first attempt to describe the process analytically. With the use of the equations presented in the modeling procedure along

with the results found for the curing kinetics, these phenomena may be incorporated into the model to examine their effect on the bubble growth rate.

Another area of interest to expand this research is in the area of complex geometry and restricted foam growth. With a final geometry containing varying thicknesses instead of a constant cross-section, the equilibrium model presented in this research may be used to determine the maximum pressure generated in the part, or the pressure in the thinnest section. The research presented on the viscosity and diffusion controlled growth was focused on unrestrained, or free rise foam growth. A further look into the foaming dynamics of constrained foam would give a more thorough understanding of the processing method employed by SAS.

REFERENCES

[1] Holder, Pat. "SPARTAN SCOUT ACTD: Unmanned Surface Vehicle (USV) for Assured Access and Force Protection. "JLOTS/Logistics-from-the-Sea Symposium. Naval Undersea Warfare Center. 4-7 February 2003.

[2] Shahat, M.F., Moawed, E.A., Burham, N. "Preparation and application of novel iminodiacetic polyurethane foam (IDA-PUF) for determination and removal of some alkali metal ions from water." *Journal of Hazardous Materials*. 160(2008): 629-633. Print.

[3] Gibson, L., Ashby, M. *Cellular Solids. Structure and Properties.* New York, NY. Cambridge University Press, 1999.

[4] Benderly, D., Rezek, Y., Zafran, J., Gorni, D. "Effect of Composition on the Fracture Toughness and Flexural Strength of Syntactic Foams." *Polymer Composites.* 25(2004): 229-236. Print.

[5] Jeon, I, Katou, K.,Sonoda,T.,Asahina,T., Kang,K. 2008. "Cell Wall Mechanical Properties of Closed-Cell Al Foam." *Mechanics of Materials*. 41(2008): 60-73. Print.

[6] Markaki and Clyne, 2001 A.E. Markaki and T.W. Clyne, "The effect of cell wall microstructure on the deformation and fracture of aluminum-based foams." *Acta Mater.* 49 (2001): 1677–1686. Print.

[7] Saha, Mrinal C,. Kabir, Md. E., Jeelani, Shaik. "Effect of Nanoparticles on Mode-I Fracture Toughness of Polyurethane Foams." *Polymer Composites.* 30(2009): 1058-1064. Print.

[8] Simone, A.E., Gibson, L.J. "The effects of cell face curvature and corrugations on the stiffness and strength of metallic foams." *Acta Mater.* 46(1998a): 3929-3935. Print.

[9] Simone, A.E., Gibson, L.J. "The effects of cell face curvature and corrugations on the stiffness and strength of metallic foams." *Acta Mater.* 46(1998a): 3929-3935. Print.

[10] Nekrasov, A.G. "Optical Method of Determining the Structural Parameters of a Polyhedral Foam." Colloid Journal. 65(2003): 757-760. Print.

[11] Marie, E., Elmoutaouakkil, A., Fazekas, A., and Salvo, L. "In Situ X-Ray Tomography Measurement of Deformation in Cellular Solids." *MRS Bull.* 28(2003): 284-289. Print.

[12] Hu, Z.W., Carlo, F. De. "Noninvasive three-dimensional visualization of defects and crack propagation in layered foam structures by phase-contrast microimaging." *Scripta Materialia.* 59(2008): 1127-1130. Print

[13] Maquet, V., Blacher, S., Pirard, R., Pirard, J.-P., and Jerome, R. "Characterization of Porour Polylactide Foams by Image Analysis and Impedance Spectroscopy." *Langmuir.* 16(2000): 10463-10470. Print.

[14]Nishioka, G.M., Ross, S., and Kornbrekke, R.E. "Fundamental Methods for Measuring Foam Stability." *Foams: Theory Measurements and Applications, Surfactant Science Series.* Marcel Dekker, New York. 57(1996): 275-285.

[15] Rhodes, R.B., and Khaykin, B. "Stereology: A Technique for the Quantitative Characterization of Foam Structure." *J Therm Insul.* 14(1991): 175-183. Print.

[16] Shih, Albert, Huang, Zhenhua. "Three-Dimensional Optical Measurements of Porous Foams." *Journal of Manufacturing Science and Engineering.* 128(2006): 951-959. Print.

[17] Center for the Polyurethanes Industry. 05 March 2010. <http://polyurethane.org/s_api/index.asp>.

[18] International Programme on Chemical Safety. 10 June 2010. <http://www.inchem.org/documents/cicads/cicads/V27CI02.gif>.

[19] Chemical Engineering Research Information Center. 8 June 2010. http://www.cheric.org/PDF/KEHH/KH03/KH03-4-0614.pdf

[20] The Role of Chemistry in History. 19 May 2010. <http://itech.dickinson.edu/chemistry/?cat=110>.

[21] About.com: Composites/Plastics. Blowing Agent. 2 February 2010. <http://composite.about.com /library/glossary/b/bldef-b712.htm>.

[22] Dow Answer Center. Polyurethane Foam Gas-Producing Reaction. 21 May 2010. <http://dow-answer.custhelp.com/app/answers/detail/a_id/5656/kw/polyurethane%20foam%20reaction >.

[23] Carlsson, L.A., Matteson, R.C., Aviles, F., Loup, D.C. "Crack path in foam cored DCB sandwich fracture specimens." *Composites Science and Technology*. 65(2005): 2612-2621. Print

[24] Chaing, Fu-Pen, Yi Ding. "Size effect on stress-strain relation of neat polyurethane foam." *Composites:Part B.* 39(2008): 42-49. Print.

[25] Clark, S.D., Shenoi, R.A., Allen, H.G. "Modeling the fatigue behavior of sandwich beams under monotonic, 2-step and block-loading regimes." *Composites Science and Technology*. 59(1999): 471-486. Print.

[26] Grenested, J.L., Hallstrom, S., Kuttenkeuler, J. "On cracks emanating from wedges in expanded PVC foam." *Engineering Fracture Mechanics*. 54(1996): 445-456. Print.

[27] Hallstrom, S., Grenestedt, J.L. "Mixed mode fracture of cracks and wedge shaped notches in expanded PVC foam." *International Journal of Fracture*. 88(1997): 343-358. Print.

[28] Jin, Helena, Wei-Yang Lu, Simon Scheffel, Terry D. Hinnerichs, and Michael K. Nelson, "Full-field characterization nof mechanical behavior of polyurethane foams." *International Journal of Solids and Structures*. 44(2007): 6930-6944. Print.

[29] Kabir, Md. E., Saha, M.C., Jeeliani, S. "Tensile and fracture behavior or polymer foams." *Materials Science and Engineering A*. 429(2006): 225-235. Print.

[30] Kulkarni, Nitin, Mahfuz, Hassan, Jeelani, Shaik, Carlsson, Leif, A. "Fatigue crack growth and life prediction of foam core sandwich composites under flexural loading." *Composite Structures*. 59(2003): 499-505. Print.

[31] Marsavina, Liviu, Sadowski, Tomasz. "Dynamic fracture toughness of polyurethane foam." *Polymer Testing*. 27(2008): 941-944. Print.

[32] Motz, C., Friedl, O., Pippan, R. "Fatigue Crack Propagation in Cellular Metals." *International Journal of Fatigue*. 27(2005): 1571-1581. Print.

[33] Noury, P.M., Shenoi, R.A., Sinclair, I. "On mixed-mode fracture of PVC foam." *International Journal of Fracture*. 92(1998): 131-151. Print.

[34] Olurin, O.B., McCullough, K.Y.G., Fleck, N.A., Ashby, M.F. "Fatigue Crack Propagation in Aluminum Alloy Foams." *International Journal of Fatigue*. 23(2001): 375-382. Print.

[35] Saint-Michel, Fabrice, Laurent Chazeau, Jean-Yves Cavaille, and Emanuelle Chabert. "Mechanical Properties of high density polyurethane foams:I. Effect of the density." *Composites Science and Technology*. 66(2006): 2700-2708. Print.

[36] Saint-Michel, Fabrice, Laurent Chazeau, and Jean-Yves Cavaille. "Mechanical properties of high density polyurethane foams: II. Effect of the filler size." *Composites Science and Technology*. 66(2006): 2709-2718. Print.

[37] Shafiq, Basir, Quispitupa, Amilcar. "Fatigue characteristics of foam core sandwich composites." *International Journal of Fatigue*. 28(2006): 96-102. Print.

[38] Sonnenschein, M., Wendt, B. "The Relationship Between Polyurethane Foam Microstructure and Foam Aging." *Polymer*. 49(2008): 934-942. Print.

[39] Trappe, V., Harbich, K.-W. "Intralaminar fatigue behavior of carbon fibre reinforced plastics." *International Journal of Fatigue*. 28(2006): 1187-1196. Print.

[40] Tu, Z.H, V.P.W. Shim, C.T. Lim. "Plastic deformation modes in rigid polyurethane foams under static loading." *International Journal of Solids and Structures*. 38(2001): 9267-9279. Print.

[41] Zenkert, Dan, Burman, Magnus. "Tension, Compression and shear fatigue of a closed cell polymer foam." *Composites Science and Technology*. 69(2009): 785-792. Print.

[42] Hailemariam, Leaelaf, Okos, Martin, Campanella, Osvaldo. "A mathematical model for the isothermal growth of bubbles in wheat dough." *Journal of Food Engineering.* 82(2007): 466-477. Print.

[43] Harikrishnan,G., Khakhar, D.V. "Effect of Monomer Temperature on Foaming and Properties of Flexible Polyurethane Foams." *Journal of Applied Polymer Science.* 105(2007): 3439-3443. Print.

[44] Matson, Douglas, Venkatesh, Rakesh, Biederman, Scott. "Expanded polystyrene lost foam casting – modeling bead steaming operations." *Journal of Manufacturing Science and Engineering.* 129(2007): 425-434. Print.

[45] Peng, S., Jackson, P., Sendijarevic, V. "Process Monitoring and Kinetics of Rigid Poly(Urethane-isocyanurate) Foams." *Journal of Applied Polymer Science.* 77(2000): 374-380. Print.

[46] Romero, R., Grigsby, R., Rister, E. "A Study of the Reaction Kinetics of Polyisocyanurate Foam Formulations using Real-time FTIR." *Journal of Cellular Plastics.* 31(2005): 349-359. Print.

[47] Taki, Kentaro. "Experimental and numerical studies on the effects of pressure release rate on number density of bubbles and bubble growth in a polymeric foaming process." *Chemical Engineering Science.* 63(2008): 3643-3653. Print.

[48] Tuladhar, T.R., Mackley, M.R. "Experimental observations and modeling relating to foaming and bubble growth from pentane loaded polystyrene melts." *Chemical Engineering Science.* 59(2004): 5997-6014. Print.

[49] Xing, Zhe, Wu, Guozhong, Huang, Shirong. "Preparation of microcellular cross-linked polyethylene foams by a radiation and supercritical carbon dioxide approach." *The Journal of Supercritical Fluids.* 47(2008): 281-289. Print.

[50] Yun, Myung Seok, Lee, Woo Il. "Analysis of bubble nucleation and growth in the pultrusion process of phenolic foam composites." *Composites Science and Technology.* 68(2008): 202-208. Print.

[51] Amon, M. (1982). *Theoretical & Experimental Study of Foam Growth Dynamics With Application to Structural Foam Molding*. Doctoral Dissertation. Department of Chemical Engineering, University of Delaware, Newark, DE.

[52] Amon, M., Denson, C.D. "A Study of the Dynamics of Foam Growth: Analysis of the Growth of Closely Spaced Spherical Bubbles." *Polymer Engineering and Science*. 24(1984): 1026-1034. Print.

[53] Bikard, J,J. Bruchon, T. Coupez, L. Silva, "Numerical simulation of 3D polyurethane expansion during manufacturing process." *Colloids and Surfaces A: Physicochem. Eng. Aspects*. 309(2007): 49-63. Print.

[54] Bruchon, J., Coupes, T. "A numerical strategy for the direct 3D simulation of the expansion of bubbles into a molten polymer during a foaming process." *International Journal for Numerical Methods in Fluids*. 57(2008): 977-1003. Print.

[55] Tekoglu, Cihan, Onck, Patrick R. "Size effects in two-dimensional Voronoi foams: A comparison between generalized continua and discrete models." *Journal of the Mechanics and Physics of Solids*. 56(2008): 3541-3564. Print.

[56] Pearson, G., Middleman, S. "Elongational Flow Behavior of Viscoelastic Liquids. Part 1: Modeling of Bubble Collapse." *IAChE Journal*. 23(1977): 714-722. Print.

[57] Rosner, D.E., Epstein, M. "Effects of Interface Kinetics Capillarity and Solute Diffusion on Bubble Growth in Highly Supersaturated Liquids." *Chemical Engineering Science*. 27(1972): 69- 88. Print.

[58] Street, J. Fricke, A., Reiss, L. "Dynamics of Phase Growth in Viscous, Non-Newtonian Liquids." *Industrial & Engineering Chemistry Fundamentals*. 10(1971): 54-64. Print.

[59] Zana, E., Leal, L.G. "The Dynamics and Dissolution of Gas Bubbles in a Viscoelastic Fluid." *International Journal of Multiphase Flow*. 4(1978): 237- 262. Print.

[60] Chemical Professionals. Calculate Diffusion Coefficients in Liquids. Chemical Professionals. 15 April 2009. <http://profmaster.blogspot.com/2009/03/calculate-diffusion-coefficient-in.html.>

[61] Dimier, F., Sbirrazzuoli, N., Vergnes, B., Vincent, M. "Curing Kinetics and Chemorheological Analysis of Polyurethane Formation." *Polymer Engineering and Science*. 44 (2004): 518-527. Print.